

1 **A toolbox for imaging RIPK1, RIPK3 and MLKL in mouse and human cells**

2

3 André L. Samson^{1,2*}, Cheree Fitzgibbon¹, Komal M. Patel¹, Joanne M. Hildebrand^{1,2}, Lachlan W.
4 Whitehead^{1,2}, Joel S. Rimes^{1,2}, Annette V. Jacobsen^{1,2}, Christopher R. Horne^{1,2}, Xavier J. Gavin^{1,2},
5 Samuel N. Young¹, Kelly L. Rogers^{1,2}, Edwin D. Hawkins^{1,2}, James M. Murphy^{1,2*}

6

7 ¹Walter and Eliza Hall Institute of Medical Research, 1G Royal Parade, Parkville, VIC 3052,
8 Australia

9 ²Department of Medical Biology, University of Melbourne, Parkville 3052, Australia

10

11 *Please address correspondence to samson.a@wehi.edu.au (ALS) or jamesm@wehi.edu.au (JMM)

12

13 Running title: Imaging necroptosis in mouse and human cells

14

15 Keywords: kinase, pseudokinase, cell death, programmed necrosis, fixative

16 **ABSTRACT**

17 Necroptosis is a lytic, inflammatory cell death pathway that is dysregulated in many human
18 pathologies. The pathway is executed by a core machinery comprising the RIPK1 and RIPK3 kinases,
19 which assemble into necrosomes in the cytoplasm, and the terminal effector pseudokinase, MLKL.
20 RIPK3-mediated phosphorylation of MLKL induces oligomerization and translocation to the plasma
21 membrane where MLKL accumulates as hotspots and perturbs the lipid bilayer to cause death. The
22 precise choreography of events in the pathway, where they occur within cells, and pathway
23 differences between species, are of immense interest. However, they have been poorly characterized
24 due to a dearth of validated antibodies for microscopy studies. Here, we describe a toolbox of
25 antibodies for immunofluorescent detection of the core necroptosis effectors, RIPK1, RIPK3 and
26 MLKL, and their phosphorylated forms, in human and mouse cells. By comparing reactivity with
27 endogenous proteins in wild-type cells and knockout controls in basal and necroptosis-inducing
28 conditions, we characterise the specificity of frequently-used commercial and recently-developed
29 antibodies for detection of necroptosis signaling events. Importantly, our findings demonstrate that
30 not all frequently-used antibodies are suitable for monitoring necroptosis by immunofluorescence
31 microscopy, and methanol- is preferable to paraformaldehyde-fixation for robust detection of specific
32 RIPK1, RIPK3 and MLKL signals.

33 INTRODUCTION

34 Cell death by necroptosis is thought to have originated as an ancestral host defence mechanism, which
35 is reflected in the breadth of pathogen-encoded proteins that inhibit the pathway^{1, 2, 3, 4, 5, 6}. In addition
36 to reported innate immunity functions^{7, 8, 9}, the dysregulation of necroptosis has been implicated in a
37 range of pathologies, including ischemic-reperfusion injuries, such as in the kidney^{10, 11} and heart¹²,
38 and inflammatory diseases^{13, 14, 15, 16}, including inflammatory bowel disease¹⁷. Accordingly, there is
39 widespread interest in therapeutically-targeting the pathway to counter human disease. Owing to the
40 recent identification of the terminal effectors of the pathway, RIPK3 (in 2009)^{1, 18, 19} and MLKL (in
41 2012)^{20, 21}, however, the extent of indications attributable to necroptotic cell death is poorly
42 understood. Precisely defining pathologies impacted by necroptosis has posed a challenge owing to
43 the dearth of antibodies validated to specifically detect members of the pathway and their activated
44 (phosphorylated) forms in fixed cells and tissues. As a result, the contribution of necroptosis to many
45 pathologies remains a subject of ongoing debate^{22, 23, 24, 25}.

46 Necroptotic cell death signaling is initiated by ligation of death receptors, such as the TNF
47 receptor 1, or pathogen detectors, such as Toll-like receptors 3 and 4 and the ZBP1/DAI intracellular
48 viral RNA sensor protein. In cellular contexts where the activities of the Inhibitors of Apoptosis
49 proteins (IAPs) E3 Ubiquitin ligase family and the proteolytic apoptotic effector, Caspase-8, are
50 depleted or compromised, necroptosis ensues. The precise choreography of necroptotic signaling is
51 still emerging, although recent studies have defined key events and checkpoints in the pathway^{26, 27,}
52 ^{28, 29}. Following pathway induction, RIPK1 autophosphorylation prompts hetero-oligomerization with
53 RIPK3 via an amyloid-forming motif in the region C-terminal to their kinase domains termed the
54 RHIM (RIP Homotypic Interaction Motif) to form a cytoplasmic platform known as the necrosome^{30,}
55 ^{31, 32}. Upon RIPK3 activation by autophosphorylation within necrosomes^{33, 34}, RIPK3 is primed to
56 phosphorylate the activation loop of the MLKL pseudokinase domain to activate MLKL's killing
57 function^{14, 20, 27, 28, 35, 36, 37, 38, 39}. In the case of human MLKL, dormant MLKL appears to be at least in

58 part pre-associated with RIPK3 in the cytoplasm^{20, 40}, and stable recruitment to necrosomes appears
59 to be an essential checkpoint in MLKL activation²⁸. In the case of mouse MLKL, a transient
60 interaction between RIPK3 and MLKL appears to be sufficient for MLKL activation in mouse cells^{35,}
61 ^{36, 37}. Regardless of species, MLKL phosphorylation is thought to provoke a conformational change
62 in the pseudokinase domain that leads to oligomerization and unmasking of the killer N-terminal
63 four-helix bundle (4HB) domain^{37, 40, 41, 42, 43}. The human MLKL 4HB domain likely engages
64 chaperones to facilitate translocation to the plasma membrane via an actin-, Golgi- and microtubule-
65 dependent mechanism, where MLKL accumulates in hotpots. When a threshold is surpassed, the 4HB
66 domains of MLKL permeabilize the membrane to induce cell death^{26, 29}.

67 While biochemical studies have defined these steps and checkpoints, visualizing the
68 spatiotemporal dynamics of endogenous proteins during in necroptosis using microscopy-based
69 approaches has proven challenging in the absence of antibodies that have been validated for target
70 specificity. Similarly, the lack of validated reagents poses a challenge to immunohistochemical
71 staining of patient tissue sections, and therefore attribution of a role for necroptosis in pathologies,
72 because knockout tissue controls are not available. Here, we have established procedures for staining
73 endogenous RIPK1, RIPK3 and MLKL, and their phosphorylated forms, in fixed mouse and human
74 cells. While several frequently-used antibodies were found to be suitable for selectively staining these
75 proteins, as validated by comparisons with cells deficient for each protein, many exhibited non-
76 specific staining and are therefore unsuitable for immunofluorescence and immunohistochemistry.
77 Our studies also highlight the importance of validating antibody compatibility with fixation methods.
78 In most cases, paraformaldehyde fixation ablated epitopes, presumably because RIPK3 and MLKL
79 are lysine-rich and prone to modification by crosslinking, whereas methanol fixation enabled specific
80 detection of these proteins. Due to the sequence divergence between mouse and human RIPK3 and
81 MLKL^{41, 43, 44, 45, 46}, it was not possible to specifically-detect proteins across species using a single
82 reagent, which necessitated the development of a new antibody that specifically detected mouse

83 MLKL. Collectively, our studies present a toolbox of selective antibodies that will enable critical
84 analysis of the chronology, checkpoints and kinetics of necroptotic signaling in mouse and human
85 cells.

86

87 **RESULTS**

88 **Immunofluorescent detection of human MLKL**

89 We recently described a monoclonal antibody, clone 10C2 (source: WEHI Antibody Facility, in-
90 house), that recognises an epitope centred on residues 413-471 of human MLKL²⁹ (Fig. 1a). The
91 initial screen that identified this clone suggested it yielded specific immunosignals when cells were
92 fixed with methanol, but not when cells were fixed with paraformaldehyde. Organic solvents such as
93 methanol preserve cells by precipitating proteins, whereas aldehyde-based agents such as
94 paraformaldehyde fix cells by crosslinking lysines and other primary amines. Because human MLKL
95 is lysine-rich (93rd percentile in the cytoplasmic and membrane-associated proteome),
96 paraformaldehyde likely causes widespread crosslinking of MLKL, which in turn masks epitopes and
97 reduces immunoreactivity. As several other necroptotic proteins are lysine-rich, we considered
98 whether the choice of fixative was a critical variable for robust immunodetection of MLKL, RIPK3
99 and RIPK1 in human and mouse cells. Accordingly, we compared the performance of 22 antibodies
100 for immunofluorescent staining of human HT29 cells and mouse dermal fibroblasts (MDFs) - two
101 cellular models that are well-characterized to undergo necroptosis when treated with TNF, Smac-
102 mimetic and IDN-6556 (herein referred to as TSI)^{5, 28, 29, 44, 47}. To quantitatively gauge the
103 performance of each antibody, their immunosignals were characterized in four ways: 1) A ratio of
104 the immunofluorescent signals between a positive and negative control. This produces a signal-to-
105 noise curve that estimates ‘specific signal abundance’ (Fig. 1b). For testing phospho-specific
106 antibodies, wild-type cells undergoing necroptosis were used as a positive control and untreated wild-
107 type cells as a negative control (Fig. S1). For testing all other antibodies, untreated wild-type cells

108 were used as a positive control and relevant knockout cells as a negative control. 2) Micrographs
109 were gated so that the minimum/maximum immunosignals corresponded to the 5th/95th percentiles of
110 the signal-to-noise curve (Fig. 1b). 3) The percentage of total signals that fall within this gate were
111 determined to show how much signal from the positive control was considered specific (Fig. 1c). 4)
112 Antibodies were immunoblotted against positive and negative controls to independently assess their
113 specificity.

114 Using this approach, we confirmed that clone 10C2 specifically detects endogenous human
115 MLKL in methanol-fixed, but not paraformaldehyde-fixed cells (Fig. 1d-f). The 10C2 clone produces
116 a favourable immunostaining profile, where the specific signals are abundant (Fig. 1e) and these
117 specific signals represent the majority of all detectable signals (Fig. 1d). We recently developed
118 another MLKL-specific antibody, clone 7G2 (source: in-house), that recognises an epitope centred
119 on α F- α G loop the C-lobe of the human MLKL pseudokinase domain, which differs to the site
120 recognised by the 10C2 clone²⁹. Despite binding a distinct site in human MLKL to 10C2, the 7G2
121 clone shows similar specificity for human MLKL in immunoblot analyses and only yields specific
122 immunofluorescent signals on methanol-fixed cells (Fig. 1d-f). Notably, clone 7G2 is inferior to clone
123 10C2 for immunofluorescence studies, because specific signals were less abundant (Fig. 1e) and were
124 a minor fraction of all detectable signals (Fig. 1d).

125 We observed that clone EPR9514 (source: Abcam), an antibody raised against phospho-S358
126 of human MLKL⁴⁸, which is a hallmark of MLKL activation during necroptosis²⁰, produced specific
127 and comparable immunofluorescent signals in both methanol- and paraformaldehyde-fixed cells
128 undergoing necroptosis (Fig. 1e). As MLKL can be disulfide-crosslinked during necroptosis^{49,50} (Fig.
129 S2A-B), we tested whether fixation in the presence of *N*-ethylmaleimide (NEM) to prevent further
130 disulfide bonding, or post-fixative treatment with Tris(2-carboxyethyl)phosphine (TCEP) to reduce
131 disulfide bonds, altered the immunofluorescent detection of phospho-MLKL by clone EPR9514.
132 However, neither preventing nor reducing disulfide bonds in fixed cells precluded the

133 immunodetection of MLKL by clone EPR9514 (Fig. S2C-D). Indeed, disulfide-crosslinking may be
134 a by-product of MLKL activation given that recombinant human MLKL oligomerizes in the absence
135 of disulfide bonds (Fig. S2E).

136 Two other anti-human MLKL antibodies were found to be non-specific (Novus Biological
137 clone 954702; and Sigma-Aldrich M6697, a polyclonal antibody raised against residues 58-70; Fig.
138 1a and 1e), with equivalent signal intensity and diffuse staining observed in wild-type and *MLKL*^{-/-}
139 cells. Lastly, immunoblotting confirmed that clones 10C2, 7G2 (both in-house) and EPR9514
140 (Abcam) were highly-specific with bands corresponding to human MLKL's molecular weight of
141 54kDa observed in wild-type but not *MLKL*^{-/-} HT29 cell lysates. In contrast, clone 954702 (Novus
142 Biological MAB9187) and the Sigma-Aldrich M6697 polyclonal antibody were non-specific, with
143 multiple bands not corresponding to the molecular weight of MLKL observed in both wild-type and
144 *MLKL*^{-/-} HT29 cell lysates (Fig. 1g).

145 In summary, three of the five antibodies that were tested selectively recognised human MLKL
146 in methanol-fixed cells (clones 10C2, 7G2 and EPR9514) and, accordingly, we recommend methanol
147 fixation for detecting endogenous human MLKL by immunofluorescence. Under these conditions,
148 cytoplasmic forms of MLKL could be detected using the 10C2 and 7G2 clones, and phospho-MLKL
149 accumulating at the cell periphery with the EPR9514 clone (Fig. 1f). These data underscore the
150 importance of careful consideration of fixation method when using MLKL as a histological marker
151 of necroptosis.

152

153 **Immunofluorescent detection of human RIPK3**

154 We next assessed five anti-human RIPK3 antibodies (Fig. 2a). Two antibodies raised against the C-
155 terminus (source: ProSci 2283, Novus Biological NBP2-24588) and one antibody raised against the
156 N-terminus of RIPK3 (source: Novus Biological MAB7604, clone 780115) yielded non-specific
157 signals via both immunofluorescence and immunoblotting (Fig. 2b-e). Our recently described

158 antibody, clone 1H2 (source: in-house)⁵, detected RIPK3 via immunofluorescence in methanol-fixed,
159 but not paraformaldehyde-fixed cells. However, most of the immunofluorescent signals produced by
160 1H2 were non-specific (Fig. 2b), and the remaining signals are specific but of very low abundance
161 (Fig. 2c). Thus, although clone 1H2 is highly-selective when used as an immunoblotting reagent (Fig.
162 2d⁵), it should only be used for the immunofluorescent detection of human RIPK3 under carefully
163 controlled conditions. Our data also showed that clone D6W2T (source: Cell Signaling Technology),
164 an antibody raised against a mark of human RIPK3 activation in necroptosis, phospho-S227,
165 produced specific immunofluorescent signals in paraformaldehyde-fixed cells undergoing
166 necroptosis, but not in methanol-fixed cells (Fig. 2d). Again, the low abundance of these specific
167 immunosignals suggests that clone D6W2T should only be used for immunofluorescence under
168 carefully controlled conditions, such as where *RIPK3*^{-/-} control cells are available for direct
169 comparison. Another caveat is that immunoblotting showed that clone D6W2T not only detected
170 RIPK3 in cells undergoing necroptosis, but also in untreated cells when RIPK3 was presumably not
171 phosphorylated at S227 (Fig. 2d). Therefore, while two of the five antibodies that were tested
172 specifically recognised human RIPK3, the low abundance of their specific signals complicates use of
173 these antibodies for studying endogenous human RIPK3 via immunofluorescence. At present, more
174 specific antibodies are needed to enable the immunofluorescent detection of human RIPK3.

175

176 **Immunofluorescent detection of human RIPK1**

177 We next tested three monoclonal anti-RIPK1 antibodies: one against the N-terminal domain (source:
178 Cell Signaling Technology clone D94C12), one against the C-terminal region (source: BD
179 Transduction Laboratories clone 38/RIP) and one raised against phospho-S166 (source: Cell
180 Signaling Technology clone D8I3A; Fig. 3a). All three clones yielded specific immunofluorescent
181 signals in methanol- and paraformaldehyde-fixed cells, however, these signals were more abundant
182 in methanol-fixed samples (Fig. 3b-d). All three clones were also specific via immunoblot (Fig. 3e).

183 Importantly, the immunosignals from clones D94C12 and 38/RIP were markedly lower in cells
184 undergoing necroptosis than in unstimulated wild-type cells (Fig. 3d-e). This observation is likely
185 due to RIPK1 undergoing widespread post-translational modification and/or proteasomal degradation
186 during TNF-induced cell death^{51,52}. Thus, despite clones D94C12 and 38/RIP exhibiting a favourable
187 immunostaining profile in unstimulated cells, their decreased reactivity in cells undergoing
188 necroptosis indicates that they should be used judiciously for immunofluorescent labelling of samples
189 for accurate analysis of necroptosis. Conversely, while clone D813A preferentially stains RIPK1 in
190 cells undergoing necroptosis, specific signals that were detected also had low intensity (Fig. 3b) and
191 low abundance (Fig. 3c). In summary, three highly-specific antibodies exist for human RIPK1.
192 However, because their specific signals have very low intensity and abundance in necroptotic cells,
193 their use for the immunofluorescent detection of RIPK1 during necroptosis should be carefully
194 controlled, including side-by-side examination of wild-type and *RIPK1*^{-/-} control cells.

195

196 **Immunofluorescent detection of mouse MLKL**

197 To our knowledge, there are currently no validated monoclonal antibodies for the immunofluorescent
198 detection for mouse MLKL in unstimulated cells. Accordingly, we raised a monoclonal antibody,
199 clone 5A6 (source: in-house), against full-length mouse MLKL (Fig. 4a). The epitope for clone 5A6
200 resides in the C-terminal domain of mouse MLKL (Fig. S3). As shown in Fig. 4a-d, clone 5A6
201 produced specific and abundant signals for endogenous mouse MLKL in methanol-fixed, but not
202 paraformaldehyde-fixed cells. Immunoblotting confirmed that clone 5A6 was highly-specific (Fig.
203 4e). Notably, compared to human MLKL which translocates en masse into cytoplasmic clusters
204 during necroptosis, the relocation of mouse MLKL into cytoplasmic clusters during necroptosis was
205 more subtle. This observation may relate to the notion that human MLKL is recruited to the
206 necrosome in a more stable manner than mouse MLKL²⁸.

207 Phosphorylation of mouse MLKL at S345 is essential for necroptosis in murine cells³⁷, and
208 therefore many antibodies have been raised against this phosphosite. We tested three commonly-used
209 antibodies (Fig. 4a-e), namely clones: EPR9515(2) (source: Abcam), 7C6.1³⁹ (source: Millipore
210 MABC1158) and D6E3G (source: Cell Signaling Technology). All three clones yielded specific
211 immunosignals in methanol-fixed cells (Fig. 4c), whereas only clone 7C6.1 was compatible with
212 paraformaldehyde fixation. However, the performance of clone D6E3G was superior to the other anti-
213 phospho-MLKL antibodies, because specific signals were more abundant (Fig. 4c) and represented a
214 higher percentage of the total detectable signal (Fig. 4b). This trend was also evident via immunoblot,
215 with clone 7C6.1 being largely non-specific, clone EPR9515(2) being moderately specific and clone
216 D6E3G exhibiting a high degree of specificity towards activated MLKL in necroptotic cells (Fig. 4e).

217 In summary, clones 5A6 and D6E3G allow the immunofluorescent detection of mouse MLKL
218 under resting and necroptotic conditions, respectively. Moreover, as with human MLKL, methanol is
219 the fixative of choice for robust immunofluorescent detection of endogenous mouse MLKL.

220

221 **Immunofluorescent detection of mouse RIPK3**

222 There are numerous well-validated antibodies raised against mouse RIPK3, including a polyclonal
223 antibody against the C-terminus (source: ProSci 2283), and monoclonal antibodies recognising
224 phospho-T231/phospho-S232 (source: Genentech clone GEN135-35-9⁵³) and the extended kinase
225 domain (residues 2-353) of mouse RIPK3 (clone 8G7⁵, in-house; Fig. 5a). These antibodies yielded
226 specific signals via both immunofluorescence and immunoblot analyses (Fig. 5b-e). Interestingly,
227 while phospho-RIPK3 concentrates into cytoplasmic clusters during necroptosis, this relocation event
228 was not detected by other, anti-total RIPK3 antibodies (Fig. 5d). This finding suggests that the
229 epitopes for RIPK3 detection are obscured via protein-protein interactions during the chronology of
230 necroptotic signaling events. To further probe the steps in the pathway, we generated another mouse
231 RIPK3 antibody, clone 1H12 (source: in-house), which has a favourable staining profile (Fig. 5b-c)

232 and which recognises the translocation of mouse RIPK3 into cytoplasmic clusters during necroptosis
233 (Fig. 5d). Notably, monoclonal antibodies raised against the N-terminal kinase domain of RIPK3,
234 8G7 and 1H12, detected several species of lower molecular weight than full length RIPK3 by
235 immunoblot. These signals are likely to be spliced isoforms of mouse RIPK3 of varying lengths, each
236 of which harbour the kinase domain antigen (residues 2-353), which are therefore not detected by
237 antibodies directed towards the C-terminus of the full-length mouse RIPK3 isoform, such as ProSci
238 2283. In summary, there are several excellent options for the immunofluorescent detection of
239 endogenous mouse RIPK3. Notably, unlike MLKL and RIPK1, the choice of fixative has no major
240 bearing on the ability to detect mouse RIPK3 by immunofluorescence (Fig. 5c).

241

242 **Immunofluorescent detection of mouse RIPK1**

243 RIPK1 exhibits greater sequence identity between mouse and human orthologs than either RIPK3 or
244 MLKL⁴¹. In keeping with this, both clone D94C12 (source: Cell Signaling Technology) and clone
245 38/RIP (source: BD Transduction Laboratories), which were raised against human RIPK1, also
246 specifically detected mouse RIPK1 via immunofluorescence and immunoblotting (Fig. 6a-e). A
247 polyclonal antibody raised against phospho-S166 of mouse RIPK1 (31122; source: Cell Signaling
248 Technology) was also found to specifically detect RIPK1 via immunoblot (Fig. 6e) and in methanol-
249 fixed, but not paraformaldehyde-fixed, cells undergoing necroptosis (Fig. 6b-d).

250 In summary, three highly-specific antibodies exist for mouse RIPK1. However, as was
251 observed in human cells, necroptosis in mouse cells causes a marked reduction in RIPK1 levels (Fig.
252 6d-e). Thus, the specific immunosignals from the antibodies tested are of low intensity and abundance
253 in necroptotic cells. Therefore, careful gating of signals is recommended for the study of mouse
254 RIPK1 in necroptotic cells.

255

256 **Antibody cocktails for imaging endogenous necroptotic signaling**

257 Having validated and compared the performance of numerous reagents, we now propose different
258 antibody combinations that can be used to study endogenous necroptotic signaling (Fig. 7a-b).
259 Because these recommendations are made to facilitate the investigation of endogenous necroptotic
260 signaling in fixed cells, we also provide an ImageJ macro to generate signal-to-noise curves for the
261 gating of specific immunosignals (Supplementary File 1). To exemplify the advantages of visualising
262 endogenous necroptotic events *in situ*, we co-stained MDFs for non-phosphorylated MLKL (clone
263 5A6; source: in-house) and phosphorylated MLKL (clone D6E3G; source: Cell Signaling
264 Technology). Similar to what was described for human MLKL²⁹, mouse MLKL was observed to
265 concentrate into cytoplasmic clusters during necroptosis. However, this compartmentalisation event
266 is less pronounced than those observed for human MLKL in necroptotic HT29 cells (arrowhead; Fig.
267 7c). Also similar to what was described for human MLKL²⁹, phosphorylated MLKL was observed to
268 form focal structures at the plasma membrane, rather than docking uniformly with the cell periphery
269 (Fig. 7c). Remarkably, although smaller than the hotspots of phosphorylated human MLKL that form
270 in necroptotic HT29 cells, junctional accumulations of phosphorylated mouse MLKL were also
271 apparent in necroptotic MDFs (Fig. 7d and Supplementary Video 1). These data suggest that the
272 assembly of both mouse and human MLKL into macromolecular structures at the plasma membrane,
273 and preferentially at sites of intercellular contact, may be an intrinsic and penultimate feature of
274 necroptotic signaling.

275

276 **DISCUSSION**

277 Here, we profiled the immunofluorescent staining of MLKL, RIPK3 and RIPK1 in fixed human and
278 mouse cells with a panel of 22 antibodies. While 17 of 22 antibodies were capable of detecting their
279 respective necroptotic protein target in fixed wild-type cells and not their knockout counterparts, only
280 14 of 22 antibodies exhibited favourable signal-to-noise for robust immunostaining (as summarized
281 in Fig. 7a).

282 The choice of fixative was a critical variable for the immunofluorescent detection of
283 necroptotic proteins. With the exception of phospho-S227 in human RIPK3 and pT231/pS232 in
284 mouse RIPK3, all other epitopes exhibited increased immunoreactivity in methanol-fixed samples.
285 Indeed, immunodetection of MLKL was often found to be entirely contingent upon the use of
286 methanol as a fixative. This observation has ramifications for the experimental and clinical
287 immunohistological detection of cell death, which is almost exclusively performed on aldehyde-fixed
288 samples. Thus, stringent antigen retrieval steps to reverse crosslinks will likely be necessary for the
289 development of a diagnostic assay for necroptosis in patient samples. High resolution microscopy is
290 also mostly performed on aldehyde-fixed cell monolayers. However, as these cell monolayers cannot
291 typically withstand antigen retrieval, we recommend the use of methanol fixation for high resolution
292 immunofluorescence of necroptosis; even though methanol fixation can be sub-optimal for both the
293 retention of certain biomolecules⁵⁴ and the preservation of cellular architecture^{55, 56}. Indeed, all but
294 one of the antibodies (source: Cell Signaling Technology clone D6W2T) in the suggested toolbox in
295 Fig. 7a are compatible with methanol fixation.

296 Our data underscore the importance of using controlled experimental conditions to maximise
297 the identification of specific immunosignals. To this end, we used wild-type cells that express high
298 levels of MLKL, RIPK3 and RIPK1, and which have a well-characterised response to necroptotic
299 stimuli. If possible, cell cultures should be fixed when low, but measurable, levels of necroptotic
300 death are occurring (Fig. S1). This is because end-stage dead cells are often lost during/after methanol
301 fixation, and because the immunosignals for phospho-RIPK1, phospho-RIPK3 and phospho-MLKL
302 peak prior to cell death²⁹. Notably, the use of knockout cells (for non-phospho-targets) or
303 unstimulated wild-type cells (for phospho-sites) as a negative control is critical, as it provides the
304 information needed to define the signal-to-noise profile of an antibody (Fig. 1b). Additionally, it is
305 also helpful if different antibodies directed toward the same target yield concordant
306 immunofluorescent signals, and if accompanying immunoblot data confirm their specificity. This

307 combined approach was important for deducing that clone D6E3G (source: Cell Signaling
308 Technology) is the best option for detecting phospho-MLKL in mouse cells (Fig. 4).

309 It is concerning that the specificity of some antibodies could not be verified. For instance,
310 while numerous studies use the ProSci 2283 antibody to detect human RIPK3^{57, 58, 59}, we found that
311 it only recognised mouse RIPK3. Similarly, M6697 (source: Sigma-Aldrich) and clone 7C6.1
312 (source: Millipore) have been widely used to respectively detect human MLKL and mouse MLKL
313 phospho-S345^{39, 60, 61, 62, 63, 64, 65}, however these reagents exhibited a low degree of specificity in our
314 hands. Nonetheless, as we did not exhaustively test the performance of these antibodies for
315 immunofluorescence using a wide variety of fixatives, blocking agents, and detergents, we cannot
316 categorically state that they are non-selective. Moreover, as ProSci 2283 (reported to detect mouse
317 and human RIPK3) and Sigma-Aldrich M6697 (reported to detect human MLKL) are polyclonal
318 antibodies, batch-to-batch variation may explain differences in their specificity between studies. It is
319 also noteworthy that the majority of monoclonal antibodies that yielded the most abundant and
320 specific signals were raised against recombinant full-length protein or component domains, rather
321 than unfolded partial domains or peptides. We reasoned that epitopes that are exposed in the cellular
322 forms of these proteins would be similarly presented within a folded protein for immune recognition
323 in the host. Phosphosite-specific antibodies differ in this regard; these were raised using linear
324 phosphopeptides and their specificity likely reflects the unstructured and solvent-exposed nature of
325 the sequences in which they reside.

326 Broadly, the specific immunosignals described in this study provide consensus about three
327 key compartmentalisation events that underlie necroptotic signaling⁶⁶. First, the core necroptotic
328 proteins - MLKL, RIPK3 and RIPK1 - predominantly reside in the cytosol under basal conditions.
329 Interestingly, rather than being diffusely distributed across the cytosol, this necroptotic machinery
330 exists as small puncta that are below the resolution limit of conventional light microscopy. It may be
331 that these necroptotic proteins are preassembled into a membrane-less organelle under basal

332 conditions. Second, RIPK1, RIPK3 and MLKL then coalesce into large cytoplasmic clusters. These
333 clusters preferentially locate to the perinuclear space and are necrosome-related as they co-stain for
334 the presence of phospho-RIPK1, -RIPK3 and -MLKL (Fig. 1-7 and ref.²⁹). It is important to note that
335 the formation of these necrosomal clusters in TSI-treated HT29 cells occurs subsequent to the
336 phosphorylation of MLKL²⁹. While these clusters likely represent a higher-order form of the
337 necrosome, the mechanisms that govern cluster formation and limit their overall size are currently
338 unknown. Third, as necroptotic signaling continues, phospho-MLKL is actively trafficked away from
339 the clusters towards the plasma membrane²⁶ where it accumulates into supramolecular assemblies
340 called “hotspots”²⁹. Recent findings suggest the release of phospho-MLKL from clusters arises from
341 MLKL undergoing a conformational change that accompanies disengagement from necrosomal
342 RIPK3⁴⁰. Our data support such a disengagement step because neither RIPK1 nor RIPK3 were
343 observed to accumulate at the plasma membrane during necroptosis in mouse or human cells (Fig. 2-
344 3 and 5-6). This disengagement step, and formation of supramolecular assemblies by both mouse and
345 human MLKL at the plasma membrane, are likely to be two additional checkpoints in necroptotic
346 signaling.

347

348 **METHODS**

349 **Materials** – Primary antibodies and the dilutions used for immunoblotting/immunofluorescence
350 were: rat anti-human MLKL (clone 10C2; produced in-house²⁹; 1:2000/1:400), rat anti-human
351 MLKL (clone 7G2; produced in-house²⁹; 1:2000/1:400), rabbit anti-phospho-S358 human MLKL
352 (Abcam ab187091; clone EPR9514; 1:2000/1:200), rat anti-mouse, human, rat, horse MLKL (clone
353 3H1; produced in-house³⁷ and available as Millipore MABC604; 1:2000/ N/A), mouse anti-phospho-
354 T357 human MLKL (Novus Biological MAB9187; clone 954702; 1:1000/1:200), rabbit anti-human
355 MLKL (Sigma-Aldrich M6697; 1:1000/1:200), rabbit anti-RIPK3 (ProSci #2283; 1:1000/1:200),
356 rabbit anti-human RIPK3 (Novus Biological NBP2-24588; 1:1000/1:200), mouse anti-human RIPK3

357 (Novus Biological; clone 780115; 1:1000/1:200), rat anti-human RIPK3 (clone 1H2; produced in-
358 house⁵ and available as Millipore MABC1640; 1:2000/1:400), rabbit anti-phospho-S227 human
359 RIPK3 (Cell Signaling Technology; clone D6W2T; 1:2000/1:200), rabbit anti-mouse or human
360 RIPK1 (Cell Signaling Technology; clone D94C12; 1:2000/1:200), mouse anti-mouse or human
361 RIPK1 (BD Biosciences; clone 38/RIP; 1:1000/1:100), rabbit anti-phospho-S166 human RIPK1 (Cell
362 Signaling Technology; clone D8I3A; 1:2000/1:200), rat anti-mouse MLKL (clone 5A6; produced in-
363 house), rabbit anti-phospho-S345 mouse MLKL (Abcam; clone EPR9515(2); 1:2000/1:200), mouse
364 anti-phospho-S345 mouse MLKL (Millipore MABC158; clone 7C6.1; 1:2000/1:200), rabbit anti-
365 phospho-S345 mouse MLKL (Cell Signaling Technology; clone D6E3G; 1:2000/1:200), rat anti-
366 mouse RIPK3 (clone 8G7; produced in-house⁵ and available from Millipore as MABC1595;
367 1:2000/1:400), rat anti-mouse RIPK3 (clone 1H12; produced in-house; 1:2000/1:400), rabbit anti-
368 phospho-T231/S232 mouse RIPK3 (Genentech; clone GEN135-35-9⁵³; 1:2000/1:400), rabbit anti-
369 phospho-S166 mouse RIPK1 (Cell Signaling Technology 31122; 1:2000/1:200), mouse anti-GAPDH
370 (Millipore MAB374; 1:2000/N/A). Secondary antibodies for immunoblotting were: horseradish
371 peroxidase (HRP)-conjugated goat anti-rat IgG (Southern Biotech 3010-05), HRP-conjugated goat
372 anti-mouse IgG (Southern Biotech 1010-05), and HRP-conjugated goat anti-rabbit IgG (Southern
373 Biotech 4010-05). All secondary antibodies for immunoblotting were used at a dilution of 1:10000.
374 Secondary immunofluorescence detection reagents were: AlexaFluor647-conjugated donkey anti-
375 rabbit IgG (ThermoFisher Scientific A31573), AlexaFluor568-conjugated donkey anti-rabbit IgG
376 (ThermoFisher Scientific A10042), AlexaFluor568-conjugated donkey anti-mouse IgG
377 (ThermoFisher Scientific A10037), AlexaFluor-594 donkey anti-rat IgG (ThermoFisher Scientific A-
378 21209), AlexaFluor488-conjugated donkey anti-rat IgG (ThermoFisher Scientific A21208). All
379 secondary antibodies for immunofluorescence were used at a dilution of 1:1000. Bond-Breaker TCEP
380 solution (ThermoFisher Scientific 77720). *N*-Ethylmaleimide (Sigma-Aldrich E3876).

381

382 **5A6 and 1H12 antibody production** – Antibodies were generated at the Walter and Eliza Hall
383 Institute Monoclonal Antibody Facility by immunizing Wistar rats with recombinant full-length
384 mouse MLKL³⁷ for clone 5A6 or recombinant mouse RIPK3 residues 2-353 for clone 1H12 and the
385 previously-reported clone 8G7⁵ that was expressed and purified from Sf21 insect cells using the
386 baculovirus expression system, before splenocytes were fused with SP2/O mouse myeloid cells and
387 arising hybridoma lines cloned. The specificity of clone 5A6 for mouse MLKL was validated via
388 immunoblot analyses as exemplified in Fig. 4e and Fig. S3. The specificity of clone 1H12 for mouse
389 RIPK3 was validated via immunoblot analyses as exemplified in Fig. 5e.

390
391 **Cell lines** – HT29 cells were provided by Mark Hampton (University of Otago). *RIPK1*^{-/-}, *RIPK3*^{-/-}
392 and *MLKL*^{-/-} HT29 cells have been previously reported^{28, 29, 67}. MDF lines were generated in-house
393 from the tails of wild-type C57BL/6J, *Mlkl*^{-/-37} and *Ripk3*^{-/-68} mice and immortalized by SV40 large T
394 antigen as reported previously^{35, 37}. The sex and precise age of these animals were not recorded,
395 although our MDFs are routinely derived from tails from 8-week-old mice. *Mlkl*^{-/-}*Ripk1*^{-/-} MDFs were
396 derived from the belly/back dermis of *Mlkl*^{-/-}*Ripk1*^{-/-} E19.5 mice¹⁶ and immortalized as described
397 above. MDF lines were generated in accordance with protocols approved by the Walter and Eliza
398 Hall Institute of Medical Research Animal Ethics Committee. Cell line identities were not further
399 validated, although their morphologies and responses to necroptotic stimuli were consistent with their
400 stated origins. Cell lines were routinely monitored to confirm they were mycoplasma-free.

401
402 **Cell culture** – HT29 cells were maintained in Dulbecco's Modified Eagle Medium (DMEM; Life
403 Technologies) containing 8% v/v heat-inactivated fetal calf serum (FCS), 2 mM L-Glutamine/-
404 GlutaMAX (ThermoFisher Scientific 35050061), 50 U ml⁻¹ penicillin and 50 U ml⁻¹ streptomycin
405 (G/P/S) under humidified 10% CO₂ at 37°C.

406

407 **Cell Treatment** – Cells were seeded into Ibi-treated 8-well μ -slides (Ibidi 80826) in media containing
408 8% v/v FCS and G/P/S at 3.0×10^4 cells per well for HT29 and 0.25×10^4 cells per well for MDFs.
409 Cells were left to adhere overnight then treated in media containing 1% v/v FCS and G/P/S and
410 supplemented with the following stimuli: 100ng/mL recombinant human TNF- α -Fc (produced in-
411 house as in ref.⁶⁹), 500nM Smac mimetic/Compound A (provided by Tetralogic Pharmaceuticals; as
412 in ref.⁷⁰), 5 μ M IDN-6556 (provided by Tetralogic Pharmaceuticals). Unless stipulated, HT29 cells
413 were stimulated for 7.5 h with TSI and MDF cells were stimulated for 90 min with TSI.

414

415 **LDH release** – Colorimetric LDH release assay kit (Promega G1780) was performed according to
416 manufacturer’s instructions.

417

418 **Whole cell lysate, SDS-PAGE, immunoblot & quantification** – Cells were lysed in ice-cold RIPA
419 buffer (10mM Tris-HCl pH 8.0, 1mM EGTA, 2mM MgCl₂, 0.5% v/v Triton X100, 0.1% w/v Na
420 deoxycholate, 0.5% w/v SDS and 90mM NaCl) supplemented with 1x Protease & Phosphatase
421 Inhibitor Cocktail (Cell Signaling Technology 5872S) and 100U/mL Benzonase (Sigma-Aldrich
422 E1014). Whole cell lysates were boiled for 10 minutes in 1 \times SDS Laemmli sample buffer (126 mM
423 Tris-HCl, pH 8, 20% v/v glycerol, 4% w/v SDS, 0.02% w/v bromophenol blue, 5% v/v 2-
424 mercaptoethanol), and resolved on 1.5mm NuPAGE 4–12% Bis-Tris gels (ThermoFisher Scientific
425 NP0335BOX) using MES Running buffer (ThermoFisher Scientific NP000202) or Bio-Rad Criterion
426 TGX 4-15% gels (Bio-Rad 5678085) using 1x TGS buffer (Bio-Rad 1610772). After transfer onto
427 nitrocellulose, membranes were blocked in 5% w/v skim milk powder in TBS-T, probed with primary
428 antibodies (see **Materials** above) then the appropriate HRP-conjugated secondary antibody (see
429 **Materials** above) and signals revealed by enhanced chemiluminescence (Merck P90720) on a
430 ChemiDoc Touch Imaging System (Bio-Rad). Between each probe, membranes were incubated in

431 stripping buffer (200mM glycine pH 2.9, 1% w/v SDS, 0.5mM TCEP) for 30 minutes at room
432 temperature then re-blocked.

433

434 ***Subcellular fractionation, BN-PAGE & immunoblot*** – HT29 cells or MDFs were seeded into 6-well
435 plates (1.0×10^6 cells per well) in media containing 8% v/v FCS and G/P/S and equilibrated overnight
436 under humidified 10% CO₂ at 37 °C conditions. Cells were then treated in media containing 1% FCS
437 and G/P/S supplemented with the agonists (as indicated above). Cells were fractionated into
438 cytoplasmic and membrane fractions³⁵. Cells were permeabilized in MELB buffer (20 mM HEPES
439 pH 7.5, 100 mM KCl, 2.5 mM MgCl₂ and 100 mM sucrose, 0.025% v/v digitonin, 2 μM N-ethyl
440 maleimide, phosphatase and protease inhibitors). Crude membrane and cytoplasmic fractions were
441 separated by centrifugation (5 minutes 11,000g), and fractions prepared in buffers to a final
442 concentration of 1% w/v digitonin. The samples were resolved on a 4–16% Bis-Tris Native PAGE
443 gel (ThermoFisher), transferred to polyvinylidene difluoride (Merck IPVH00010). After transfer,
444 membranes were destained (in 50% (v/v) methanol, 25% (v/v) acetic acid), denatured (in 6M
445 Guanidine hydrochloride, 10 mM Tris pH6.8, 5 mM β-mercaptoethanol), blocked in 5% skim milk
446 (Diploma), and probed in the same manner as above.

447

448 ***Protein production and purification*** – Full-length human and mouse MLKL and the C-terminal,
449 pseudokinase domain of mouse and human MLKL were expressed in Sf21 insect cells using the Bac-
450 to-Bac system (ThermoFisher Scientific) and purified using established procedures^{28, 37, 42}. Briefly,
451 proteins were expressed with an N-terminal, TEV protease-cleavable GST (full length human MLKL)
452 or His₆ (full length mouse MLKL and pseudokinase domains) tags and captured from lysates using
453 glutathione resin (UBP Bio) or HisTag Ni-NTA resin (Roche) respectively. Proteins were cleaved
454 on-resin from the GST tag or off-resin for His₆ tags using His-tagged TEV protease, before protease
455 was removed by Ni-NTA chromatography (HisTag resin, Roche). Protein was concentrated by

456 centrifugal ultrafiltration and applied to a Superdex-200 (GE Healthcare) size exclusion
457 chromatography column; protein was eluted in 20 mM HEPES pH 7.5, 200 mM NaCl, 5% v/v
458 glycerol. Protein containing fractions were spin concentrated to 5-10 mg/mL, aliquoted, snap frozen
459 in liquid N₂ and stored at -80°C until required.

460

461 ***Immunofluorescence*** – Cells in 8-well μ -Slides (Ibidi 80826) were ice-chilled for 3 minutes, then
462 washed in ice-cold Dulbecco's PBS (dPBS; ThermoFisher Scientific 14190144), then fixed for 30
463 minutes in either ice-cold methanol or ice-cold 4% w/v PFA. Cells were washed twice in ice-cold
464 dPBS, then blocked in ice-cold Tris-balanced salt solution with 0.05% v/v Triton-X100 (TBS-T)
465 supplemented with 10% v/v donkey serum (Sigma-Aldrich D9663) for >1 hour. Cells were incubated
466 in primary antibodies (see ***Materials*** above) overnight at 4 °C in TBS-T with 10% v/v donkey serum.
467 Cells were washed twice in TBS-T then incubated in the appropriate secondary antibodies
468 supplemented with 0.1 μ g/mL Hoechst 33342 (ThermoFisher Scientific H3570) for 3 hours at room
469 temperature with gentle rocking. Cells were washed four times in ice-cold TBS-T then stored at 4 °C
470 until imaged. Where indicated, to demarcate the plasma membrane, 2 μ L of biotinylated wheat germ
471 agglutinin (Sigma-Aldrich L5142) was added to each well 10 minutes before fixation. The fixed
472 wheat germ agglutinin was then detected via the addition of 1:1000 dilution of DyLight650-
473 conjugated streptavidin (ThermoFisher Scientific 84547) during the secondary antibody incubation
474 step.

475

476 ***Two-dimensional epifluorescence microscopy*** - Samples in TBS-T were imaged on an Inverted Axio
477 Observer.Z1 microscope (Zeiss) with the following specifications: C-Apochromat 40x/1.20 W
478 autocorr UV VIS IR lens, HXP 120V excitation source, AlexaFluor647 and DyLight650 imaged with
479 a $\lambda_{\text{Excitation}}=625\text{-}655\text{nm}$; $\lambda_{\text{beamsplitter}}=660\text{nm}$; $\lambda_{\text{Emission}}=665\text{-}715\text{nm}$ filter, AlexaFluor568 imaged with a
480 $\lambda_{\text{Excitation}}=532\text{-}544\text{nm}$; $\lambda_{\text{beamsplitter}}=560\text{nm}$; $\lambda_{\text{Emission}}=573\text{-}613\text{nm}$, AlexaFluor488 imaged with a

481 $\lambda_{\text{Excitation}}=450\text{-}490\text{nm}$; $\lambda_{\text{beamsplitter}}=495\text{nm}$; $\lambda_{\text{Emission}}=500\text{-}550\text{nm}$, Hoechst 33342 imaged with a
482 $\lambda_{\text{Excitation}}=359\text{-}371\text{nm}$; $\lambda_{\text{beamsplitter}}=395\text{nm}$; $\lambda_{\text{Emission}}=397\text{-}\infty\text{ nm}$, a sCMOS PCO.edge 4.2 camera, ZEN
483 blue 2.5 pro capture software and ImageJ 1.53c post-acquisition processing software⁷¹. Typically, for
484 each independent experiment, 5-10 randomly selected fields were captured per treatment group,
485 whereby only the Hoechst 33342 signal was visualised prior to multi-channel acquisition. To ensure
486 consistent signal intensities across independent experiments, the same excitation, emission and
487 camera settings were used throughout this study.

488

489 ***Airyscan microscopy*** – Fixed immunostained cells in 8-well μ -Slides (Ibidi 80827) were subjected
490 to super-resolution 3-dimensional Airyscan microscopy on an Inverted LSM 880 platform (Zeiss)
491 equipped with the following specifications: a 63x/1.4 N.A. PlanApo DIC M27 oil immersion
492 objective (Zeiss), 405-, 488-, 568- and 640-nm laser lines, and radially-stacked Airyscan GaASP
493 detectors set to SR-mode, 405-, 488-, 561-, 633-nm laser lines and ZEN black 2.3 SP1 FP3 v14.0
494 capture software. Image stacks were acquired with a z-step size of 159nm. Super-resolution
495 deconvolution was performed using the automated ‘3D AiryScan Processing’ function of ZEN blue
496 software.

497

498 ***Hotspot quantitation*** – Micrographs (captured as in *two-dimensional epifluorescence microscopy*)
499 were opened in ImageJ 1.53c⁷¹. A rolling ball filter of 7 was applied and phospho-S358 MLKL
500 immunosignals thresholded (≥ 7000 units) and objects segmented using the ‘Analyze>Analyze
501 Particles’ tool. Segmented objects with size $0.5\text{-}100\mu\text{m}^2$ and feret diameter >2 (i.e. elliptical objects)
502 were considered hotspots. The number of segmented objects per 100 cells was taken as an index of
503 hotspot occurrence. The mean size of the segmented objects was taken as an index of hotspot size.
504 The fluorescence intensity of each segmented object divided by its size was taken as an index of
505 hotspot intensity.

506

507 **ACKNOWLEDGEMENTS**

508 We thank the Walter and Eliza Hall Institute Monoclonal Antibody Facility for their assistance
509 generating clones 3H1, 10C2, 7G2, 1H2, 5A6, 8G7 and 1H12; and Cathrine Hall for assistance
510 generating *Mkl^{-/-} Ripk1^{-/-}* MDF lines. We are grateful to the Australian National Health and Medical
511 Research Council for fellowship (J.M.H., 1142669; E.D.H., 1159488; J.M.M., 1172929), grant
512 (1124735, 1124737, and 1105023), and infrastructure (IRIISS 9000587) support, with additional
513 support from the CASS Foundation (A.L.S.) and the Victorian Government Operational
514 Infrastructure Support scheme. We acknowledge the support for A.V.J. from an Australian Research
515 Training Program Scholarship.

516

517 **AUTHOR CONTRIBUTIONS**

518 Investigation: A.L.S., K.P., C.F., J.M.H., L.W., J.R., A.V.J., C.R.H., X.G., S.N.Y. Supervision and
519 Methodology: A.L.S., J.M.H., K.L.R., E.D.H. and J.M.M.; Conceptualization: A.L.S., E.D.H. and
520 J.M.M.; Writing – Original Draft: A.L.S. and J.M.M.; Writing – Review & Editing: all authors.

521

522 **COMPETING INTERESTS**

523 A.L.S., K.P. C.F., J.M.H., S.N.Y. and J.M.M. contribute to a project developing necroptosis inhibitors
524 in collaboration with Anaxis Pharma. The other authors declare no competing interests.

525

526 **MATERIALS REQUESTS**

527 All materials will be provided under Materials Transfer Agreement upon request to James Murphy
528 (jamesm@wehi.edu.au).

529

530 **REFERENCES**

531

- 532 1. Cho YS, Challa S, Moquin D, Genga R, Ray TD, Guildford M, *et al.* Phosphorylation-driven
533 assembly of the RIP1-RIP3 complex regulates programmed necrosis and virus-induced
534 inflammation. *Cell* 2009, **137**(6): 1112-1123.
535
- 536 2. Guo H, Omoto S, Harris PA, Finger JN, Bertin J, Gough PJ, *et al.* Herpes simplex virus
537 suppresses necroptosis in human cells. *Cell Host Microbe* 2015, **17**(2): 243-251.
538
- 539 3. Pearson JS, Giogha C, Muhlen S, Nachbur U, Pham CL, Zhang Y, *et al.* EspL is a bacterial
540 cysteine protease effector that cleaves RHIM proteins to block necroptosis and inflammation.
541 *Nat Microbiol* 2017, **2**: 16258.
542
- 543 4. Pearson JS, Murphy JM. Down the rabbit hole: Is necroptosis truly an innate response to
544 infection? *Cell Microbiol* 2017, **19**(8): e12750.
545
- 546 5. Petrie EJ, Sandow JJ, Lehmann WIL, Liang LY, Coursier D, Young SN, *et al.* Viral MLKL
547 Homologs Subvert Necroptotic Cell Death by Sequestering Cellular RIPK3. *Cell reports*
548 2019, **28**(13): 3309-3319 e3305.
549
- 550 6. Fletcher-Etherington A, Nobre L, Nightingale K, Antrobus R, Nichols J, Davison AJ, *et al.*
551 Human cytomegalovirus protein pUL36: A dual cell death pathway inhibitor. *Proc Natl Acad*
552 *Sci U S A* 2020, **117**(31): 18771-18779.
553
- 554 7. Kitur K, Wachtel S, Brown A, Wickersham M, Paulino F, Penaloza HF, *et al.* Necroptosis
555 Promotes Staphylococcus aureus Clearance by Inhibiting Excessive Inflammatory Signaling.
556 *Cell reports* 2016, **16**(8): 2219-2230.
557
- 558 8. Shubina M, Tummers B, Boyd DF, Zhang T, Yin C, Gautam A, *et al.* Necroptosis restricts
559 influenza A virus as a stand-alone cell death mechanism. *J Exp Med* 2020, **217**(11).
560
- 561 9. Simpson J, Loh Z, Ullah MA, Lynch JP, Werder RB, Collinson N, *et al.* Respiratory Syncytial
562 Virus Infection Promotes Necroptosis and HMGB1 Release by Airway Epithelial Cells. *Am*
563 *J Respir Crit Care Med* 2020, **201**(11): 1358-1371.
564

- 565 10. Muller T, Dewitz C, Schmitz J, Schroder AS, Brasen JH, Stockwell BR, *et al.* Necroptosis
566 and ferroptosis are alternative cell death pathways that operate in acute kidney failure. *Cell*
567 *Mol Life Sci* 2017, **74**(19): 3631-3645.
568
- 569 11. Pefanis A, Ierino FL, Murphy JM, Cowan PJ. Regulated necrosis in kidney ischemia-
570 reperfusion injury. *Kidney Int* 2019, **96**(2): 291-301.
571
- 572 12. Luedde M, Lutz M, Carter N, Sosna J, Jacoby C, Vucur M, *et al.* RIP3, a kinase promoting
573 necroptotic cell death, mediates adverse remodelling after myocardial infarction. *Cardiovasc*
574 *Res* 2014, **103**(2): 206-216.
575
- 576 13. Hildebrand JM, Kauppi M, Majewski IJ, Liu Z, Cox AJ, Miyake S, *et al.* A missense mutation
577 in the MLKL brace region promotes lethal neonatal inflammation and hematopoietic
578 dysfunction. *Nat Commun* 2020, **11**(1): 3150.
579
- 580 14. Wang H, Sun L, Su L, Rizo J, Liu L, Wang LF, *et al.* Mixed Lineage Kinase Domain-like
581 Protein MLKL Causes Necrotic Membrane Disruption upon Phosphorylation by RIP3. *Mol*
582 *Cell* 2014, **54**(1): 133-146.
583
- 584 15. Rickard JA, Anderton H, Etemadi N, Nachbur U, Darding M, Peltzer N, *et al.* TNFR1-
585 dependent cell death drives inflammation in Sharpin-deficient mice. *Elife* 2014, **3**: e03464.
586
- 587 16. Rickard JA, O'Donnell JA, Evans JM, Lalaoui N, Poh AR, Rogers TW, *et al.* RIPK1 regulates
588 RIPK3-MLKL driven systemic inflammation and emergency hematopoiesis. *Cell* 2014,
589 **157**(2): 1175-1188.
590
- 591 17. Pierdomenico M, Negroni A, Stronati L, Vitali R, Prete E, Bertin J, *et al.* Necroptosis is active
592 in children with inflammatory bowel disease and contributes to heighten intestinal
593 inflammation. *Am J Gastroenterol* 2014, **109**(2): 279-287.
594
- 595 18. He S, Wang L, Miao L, Wang T, Du F, Zhao L, *et al.* Receptor interacting protein kinase-3
596 determines cellular necrotic response to TNF-alpha. *Cell* 2009, **137**(6): 1100-1111.
597

- 598 19. Zhang DW, Shao J, Lin J, Zhang N, Lu BJ, Lin SC, *et al.* RIP3, an energy metabolism
599 regulator that switches TNF-induced cell death from apoptosis to necrosis. *Science* 2009,
600 **325**(5938): 332-336.
601
- 602 20. Sun L, Wang H, Wang Z, He S, Chen S, Liao D, *et al.* Mixed lineage kinase domain-like
603 protein mediates necrosis signaling downstream of RIP3 kinase. *Cell* 2012, **148**(1-2): 213-
604 227.
605
- 606 21. Zhao J, Jitkaew S, Cai Z, Choksi S, Li Q, Luo J, *et al.* Mixed lineage kinase domain-like is a
607 key receptor interacting protein 3 downstream component of TNF-induced necrosis. *Proc*
608 *Natl Acad Sci U S A* 2012, **109**(14): 5322-5327.
609
- 610 22. Wang T, Perera ND, Chiam MDF, Cuic B, Wanniarachchillage N, Tomas D, *et al.*
611 Necroptosis is dispensable for motor neuron degeneration in a mouse model of ALS. *Cell*
612 *Death Differ* 2019.
613
- 614 23. Dermentzaki G, Politi KA, Lu L, Mishra V, Perez-Torres EJ, Sosunov AA, *et al.* Deletion of
615 Ripk3 Prevents Motor Neuron Death In Vitro but not In Vivo. *eNeuro* 2019, **6**(1).
616
- 617 24. Dominguez S, Varfolomeev E, Brendza R, Stark K, Tea J, Imperio J, *et al.* Genetic
618 inactivation of RIP1 kinase does not ameliorate disease in a mouse model of ALS. *Cell Death*
619 *Differ* 2020.
620
- 621 25. Dara L, Johnson H, Suda J, Win S, Gaarde W, Han D, *et al.* Receptor interacting protein
622 kinase 1 mediates murine acetaminophen toxicity independent of the necrosome and not
623 through necroptosis. *Hepatology* 2015, **62**(6): 1847-1857.
624
- 625 26. Petrie EJ, Birkinshaw RW, Koide A, Denbaum E, Hildebrand JM, Garnish SE, *et al.*
626 Identification of MLKL membrane translocation as a checkpoint in necroptotic cell death
627 using Monobodies. *Proc Natl Acad Sci U S A* 2020, **117**(15): 8468-8475.
628
- 629 27. Petrie EJ, Czabotar PE, Murphy JM. The Structural Basis of Necroptotic Cell Death
630 Signaling. *Trends Biochem Sci* 2019, **44**(1): 53-63.
631

- 632 28. Petrie EJ, Sandow JJ, Jacobsen AV, Smith BJ, Griffin MDW, Lucet IS, *et al.* Conformational
633 switching of the pseudokinase domain promotes human MLKL tetramerization and cell death
634 by necroptosis. *Nat Commun* 2018, **9**(1): 2422.
635
- 636 29. Samson AL, Zhang Y, Geoghegan ND, Gavin XJ, Davies KA, Mlodzianoski MJ, *et al.* MLKL
637 trafficking and accumulation at the plasma membrane control the kinetics and threshold for
638 necroptosis. *Nat Commun* 2020, **11**(1): 3151.
639
- 640 30. Li J, McQuade T, Siemer AB, Napetschnig J, Moriwaki K, Hsiao YS, *et al.* The RIP1/RIP3
641 necrosome forms a functional amyloid signaling complex required for programmed necrosis.
642 *Cell* 2012, **150**(2): 339-350.
643
- 644 31. Mompean M, Li W, Li J, Laage S, Siemer AB, Bozkurt G, *et al.* The Structure of the
645 Necrosome RIPK1-RIPK3 Core, a Human Hetero-Amyloid Signaling Complex. *Cell* 2018,
646 **173**(5): 1244-1253 e1210.
647
- 648 32. Sun X, Yin J, Starovasnik MA, Fairbrother WJ, Dixit VM. Identification of a novel homotypic
649 interaction motif required for the phosphorylation of receptor-interacting protein (RIP) by
650 RIP3. *J Biol Chem* 2002, **277**(11): 9505-9511.
651
- 652 33. Cook WD, Moujalled DM, Ralph TJ, Lock P, Young SN, Murphy JM, *et al.* RIPK1- and
653 RIPK3-induced cell death mode is determined by target availability. *Cell Death Differ* 2014,
654 **21**(10): 1600-1612.
655
- 656 34. Orozco S, Yatim N, Werner MR, Tran H, Gunja SY, Tait SW, *et al.* RIPK1 both positively
657 and negatively regulates RIPK3 oligomerization and necroptosis. *Cell Death Differ* 2014,
658 **21**(10): 1511-1521.
659
- 660 35. Hildebrand JM, Tanzer MC, Lucet IS, Young SN, Spall SK, Sharma P, *et al.* Activation of
661 the pseudokinase MLKL unleashes the four-helix bundle domain to induce membrane
662 localization and necroptotic cell death. *Proc Natl Acad Sci U S A* 2014, **111**(42): 15072-
663 15077.
664

- 665 36. Murphy JM. The Killer Pseudokinase Mixed Lineage Kinase Domain-Like Protein (MLKL).
666 *Cold Spring Harb Perspect Biol* 2020, **12**(8).
667
- 668 37. Murphy JM, Czabotar PE, Hildebrand JM, Lucet IS, Zhang JG, Alvarez-Diaz S, *et al.* The
669 pseudokinase MLKL mediates necroptosis via a molecular switch mechanism. *Immunity*
670 2013, **39**(3): 443-453.
671
- 672 38. Tanzer MC, Tripaydonis A, Webb AI, Young SN, Varghese LN, Hall C, *et al.* Necroptosis
673 signalling is tuned by phosphorylation of MLKL residues outside the pseudokinase domain
674 activation loop. *The Biochemical journal* 2015, **471**(2): 255-265.
675
- 676 39. Rodriguez DA, Weinlich R, Brown S, Guy C, Fitzgerald P, Dillon CP, *et al.* Characterization
677 of RIPK3-mediated phosphorylation of the activation loop of MLKL during necroptosis. *Cell*
678 *Death Differ* 2016, **23**(1): 76-88.
679
- 680 40. Garnish SE, Meng Y, Koide A, Sandow JJ, Denbaum E, Jacobsen AV, *et al.* Conformational
681 interconversion of MLKL and disengagement from RIPK3 precedes cell death by necroptosis.
682 Under review.
683
- 684 41. Davies KA, Fitzgibbon C, Young SN, Garnish SE, Yeung W, Coursier D, *et al.* Distinct
685 pseudokinase domain conformations underlie divergent activation mechanisms among
686 vertebrate MLKL orthologues. *Nat Commun* 2020, **11**(1): 3060.
687
- 688 42. Murphy JM, Lucet IS, Hildebrand JM, Tanzer MC, Young SN, Sharma P, *et al.* Insights into
689 the evolution of divergent nucleotide-binding mechanisms among pseudokinases revealed by
690 crystal structures of human and mouse MLKL. *The Biochemical journal* 2014, **457**(3): 369-
691 377.
692
- 693 43. Tanzer MC, Matti I, Hildebrand JM, Young SN, Wardak A, Tripaydonis A, *et al.*
694 Evolutionary divergence of the necroptosis effector MLKL. *Cell Death Differ* 2016, **23**(7):
695 1185-1197.
696

- 697 44. Davies KA, Tanzer MC, Griffin MDW, Mok YF, Young SN, Qin R, *et al.* The brace helices
698 of MLKL mediate interdomain communication and oligomerisation to regulate cell death by
699 necroptosis. *Cell Death Differ* 2018, **25**(9): 1567-1580.
700
- 701 45. Dondelinger Y, Hulpiau P, Saeys Y, Bertrand MJM, Vandenabeele P. An evolutionary
702 perspective on the necroptotic pathway. *Trends Cell Biol* 2016, **26**(10): 721-732.
703
- 704 46. Newton K, Manning G. Necroptosis and Inflammation. *Annu Rev Biochem* 2016, **85**: 743-
705 763.
706
- 707 47. Petrie EJ, Birkinshaw RW, Koide A, Denbaum E, Hildebrand JM, Garnish SE, *et al.*
708 Identification of MLKL membrane translocation as a checkpoint in necroptotic cell death
709 using Monobodies. *Proc Natl Acad Sci U S A* 2020.
710
- 711 48. Wang H, Sun L, Su L, Rizo J, Liu L, Wang LF, *et al.* Mixed lineage kinase domain-like
712 protein MLKL causes necrotic membrane disruption upon phosphorylation by RIP3. *Mol Cell*
713 2014, **54**(1): 133-146.
714
- 715 49. Cai Z, Jitkaew S, Zhao J, Chiang HC, Choksi S, Liu J, *et al.* Plasma membrane translocation
716 of trimerized MLKL protein is required for TNF-induced necroptosis. *Nature cell biology*
717 2014, **16**(1): 55-65.
718
- 719 50. Chen X, Li W, Ren J, Huang D, He WT, Song Y, *et al.* Translocation of mixed lineage kinase
720 domain-like protein to plasma membrane leads to necrotic cell death. *Cell research* 2014,
721 **24**(1): 105-121.
722
- 723 51. Alturki NA, McComb S, Ariana A, Rijal D, Korneluk RG, Sun SC, *et al.* Triad3a induces the
724 degradation of early necrosome to limit RipK1-dependent cytokine production and
725 necroptosis. *Cell Death Dis* 2018, **9**(6): 592.
726
- 727 52. Simpson DS, Gabrielyan A, Feltham R. RIPK1 ubiquitination: Evidence, correlations and the
728 undefined. *Semin Cell Dev Biol* 2020.
729

- 730 53. Newton K, Wickliffe KE, Maltzman A, Dugger DL, Strasser A, Pham VC, *et al.* RIPK1
731 inhibits ZBP1-driven necroptosis during development. *Nature* 2016, **540**(7631): 129-133.
732
- 733 54. Hoetelmans RW, Prins FA, Cornelese-ten Velde I, van der Meer J, van de Velde CJ, van
734 Dierendonck JH. Effects of acetone, methanol, or paraformaldehyde on cellular structure,
735 visualized by reflection contrast microscopy and transmission and scanning electron
736 microscopy. *Appl Immunohistochem Mol Morphol* 2001, **9**(4): 346-351.
737
- 738 55. Moloney M, McDonnell L, O'Shea H. Atomic force microscopy of BHK-21 cells: an
739 investigation of cell fixation techniques. *Ultramicroscopy* 2004, **100**(3-4): 153-161.
740
- 741 56. Whelan DR, Bell TD. Correlative Synchrotron Fourier Transform Infrared Spectroscopy and
742 Single Molecule Super Resolution Microscopy for the Detection of Composition and
743 Ultrastructure Alterations in Single Cells. *ACS Chem Biol* 2015, **10**(12): 2874-2883.
744
- 745 57. Xu X, Kalac M, Markson M, Chan M, Brody JD, Bhagat G, *et al.* Reversal of CYLD
746 phosphorylation as a novel therapeutic approach for adult T-cell leukemia/lymphoma
747 (ATLL). *Cell Death Dis* 2020, **11**(2): 94.
748
- 749 58. Yang C, Li J, Yu L, Zhang Z, Xu F, Jiang L, *et al.* Regulation of RIP3 by the transcription
750 factor Sp1 and the epigenetic regulator UHRF1 modulates cancer cell necroptosis. *Cell Death*
751 *Dis* 2017, **8**(10): e3084.
752
- 753 59. Wang S, Ni HM, Dorko K, Kumer SC, Schmitt TM, Nawabi A, *et al.* Increased hepatic
754 receptor interacting protein kinase 3 expression due to impaired proteasomal functions
755 contributes to alcohol-induced steatosis and liver injury. *Oncotarget* 2016, **7**(14): 17681-
756 17698.
757
- 758 60. Zhang S, Che L, He C, Huang J, Guo N, Shi J, *et al.* Drp1 and RB interaction to mediate
759 mitochondria-dependent necroptosis induced by cadmium in hepatocytes. *Cell Death Dis*
760 2019, **10**(7): 523.
761
- 762 61. Ali M, Mocarski ES. Proteasome inhibition blocks necroptosis by attenuating death complex
763 aggregation. *Cell Death Dis* 2018, **9**(3): 346.

764

765 62. Gong YN, Guy C, Olauson H, Becker JU, Yang M, Fitzgerald P, *et al.* ESCRT-III Acts
766 Downstream of MLKL to Regulate Necroptotic Cell Death and Its Consequences. *Cell* 2017,
767 **169**(2): 286-300 e216.

768

769 63. Yoon S, Bogdanov K, Kovalenko A, Wallach D. Necroptosis is preceded by nuclear
770 translocation of the signaling proteins that induce it. *Cell Death Differ* 2016, **23**(2): 253-260.

771

772 64. Wang Z, Jiang H, Chen S, Du F, Wang X. The mitochondrial phosphatase PGAM5 functions
773 at the convergence point of multiple necrotic death pathways. *Cell* 2012, **148**(1-2): 228-243.

774

775 65. Mizumura K, Cloonan SM, Nakahira K, Bhashyam AR, Cervo M, Kitada T, *et al.* Mitophagy-
776 dependent necroptosis contributes to the pathogenesis of COPD. *J Clin Invest* 2014, **124**(9):
777 3987-4003.

778

779 66. Samson AL, Garnish SE, Hildebrand JM, Murphy JM. Location, location, location: a
780 compartmentalized view of necroptotic signaling. Under review.

781

782 67. Tanzer MC, Khan N, Rickard JA, Etemadi N, Lalaoui N, Spall SK, *et al.* Combination of IAP
783 antagonist and IFN γ activates novel caspase-10- and RIPK1-dependent cell death
784 pathways. *Cell Death Differ* 2017, **24**(3): 481-491.

785

786 68. Newton K, Sun X, Dixit VM. Kinase RIP3 is dispensable for normal NF-kappa Bs, signaling
787 by the B-cell and T-cell receptors, tumor necrosis factor receptor 1, and Toll-like receptors 2
788 and 4. *Mol Cell Biol* 2004, **24**(4): 1464-1469.

789

790 69. Bossen C, Ingold K, Tardivel A, Bodmer JL, Gaide O, Hertig S, *et al.* Interactions of tumor
791 necrosis factor (TNF) and TNF receptor family members in the mouse and human. *J Biol*
792 *Chem* 2006, **281**(20): 13964-13971.

793

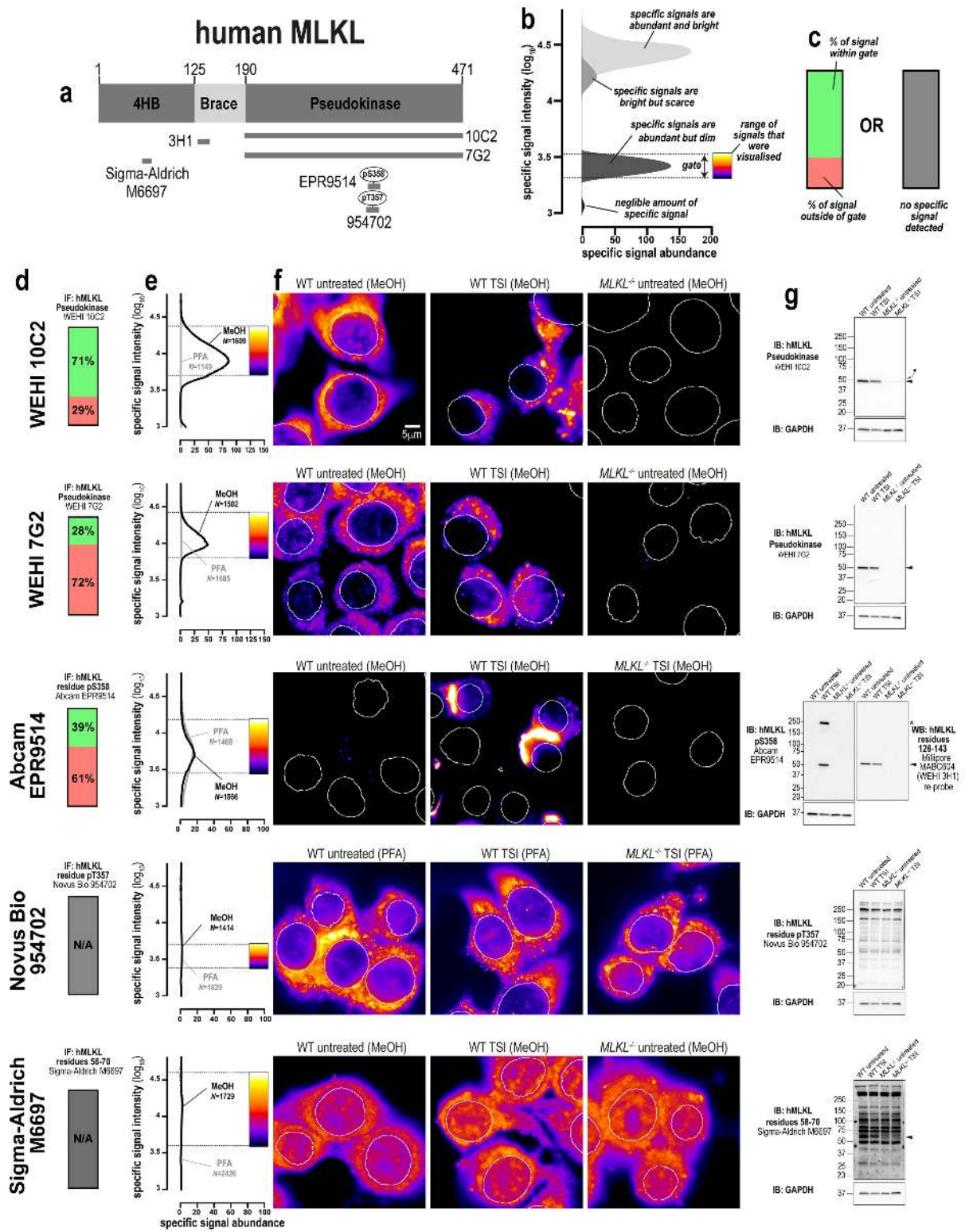
794 70. Vince JE, Wong WW, Khan N, Feltham R, Chau D, Ahmed AU, *et al.* IAP antagonists target
795 cIAP1 to induce TNF α -dependent apoptosis. *Cell* 2007, **131**(4): 682-693.

796

- 797 71. Schneider CA, Rasband WS, Eliceiri KW. NIH Image to ImageJ: 25 years of image analysis.
798 *Nat Methods* 2012, **9**(7): 671-675.
799
800

801 FIGURES LEGENDS

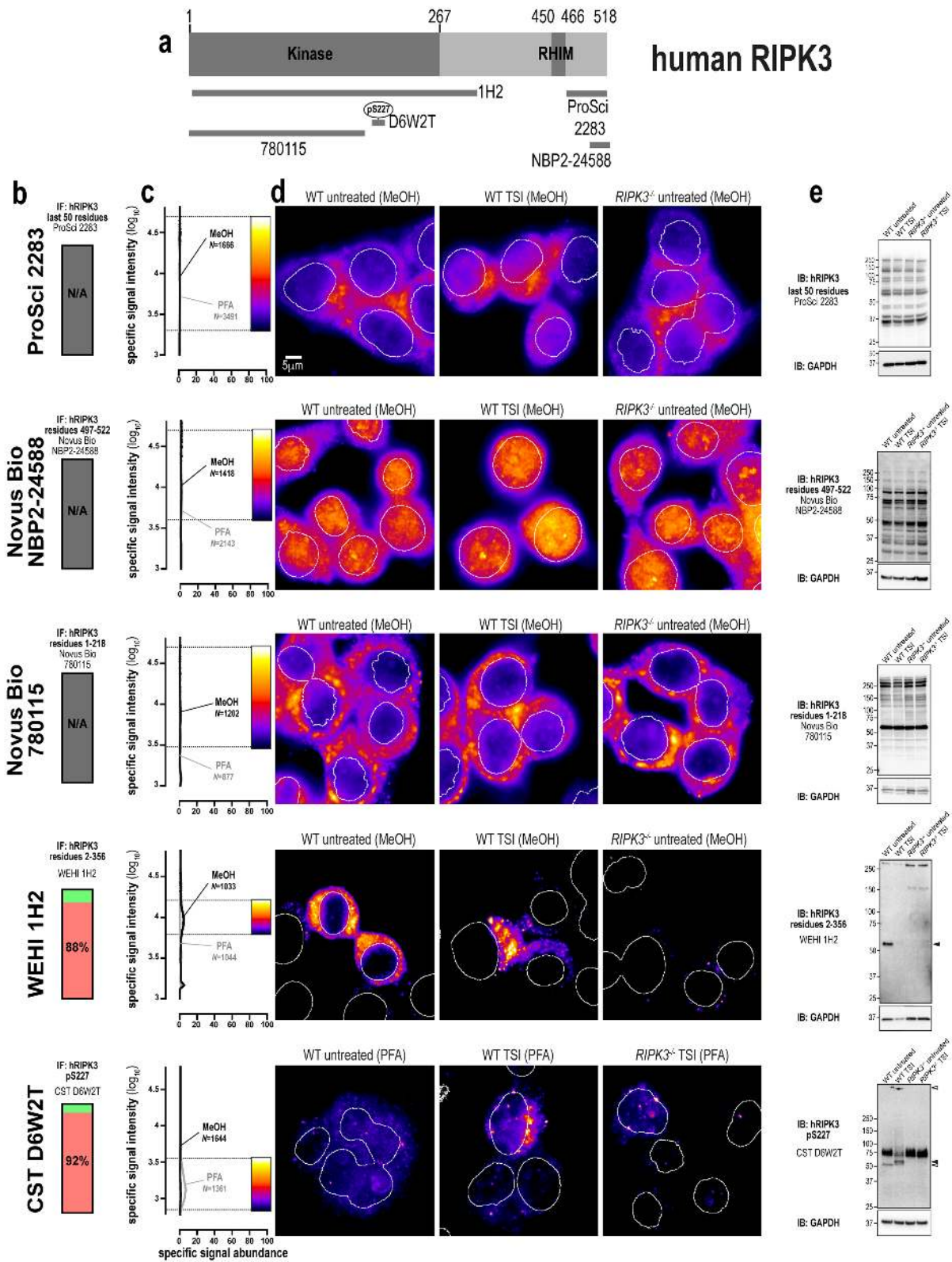
Figure 1



802

803 **Figure 1: Methanol fixation is optimal for the immunofluorescent detection of human MLKL**
804 **a** Human MLKL domain architecture showing the immunogens used to raise the tested anti-MLKL
805 antibodies. **b** Demonstration of how signal-to-noise ratios were used to quantify the abundance and
806 brightness of specific immunofluorescent signals generated by different antibodies. The 5th and 95th
807 percentile of each signal-to-noise curve defines the gate where specific immunosignals were
808 observed. As indicated by the pseudocolour look-up-table, only immunosignals within this gate were
809 visualised. **c** Chart exemplifying how the amount of signal within the gate, relative to the total amount
810 of detectable signal, provides another gauge of antibody specificity for immunofluorescence. **d**
811 Quantitation of the percentage of gated signals for the tested MLKL antibodies. **e** Quantitation of
812 specific signal abundance produced by the tested MLKL antibodies on methanol-fixed (MeOH) or
813 paraformaldehyde-fixed (PFA) HT29 cells. The number of cells imaged (N) to generate each signal-
814 to-noise curve is shown. **f** Micrographs of immunofluorescent signals for the tested MLKL antibodies
815 on HT29 cells. As indicated by each pseudocolour look-up-table, only immunosignals within the
816 respective gate in panel **e** were visualised. Data are representative of n=3 (clones 10C2, 7G2) and
817 n=2 (Abcam clone EPR9514, Novus Biological MAB9187/clone 954702 and Sigma-Aldrich M6697)
818 independent experiments. Nuclei were detected by Hoechst 33342 staining and are demarked by
819 white outlines in micrographs. **g** Immunoblot using the tested MLKL antibodies against wild-type
820 and *MLKL*^{-/-} HT29 cell lysates. Closed arrowheads indicate the main specific band. Asterisks indicate
821 non-specific bands that could otherwise confound data interpretation. Immunoblots were re-probed
822 for GAPDH as loading control.
823

Figure 2



824

825

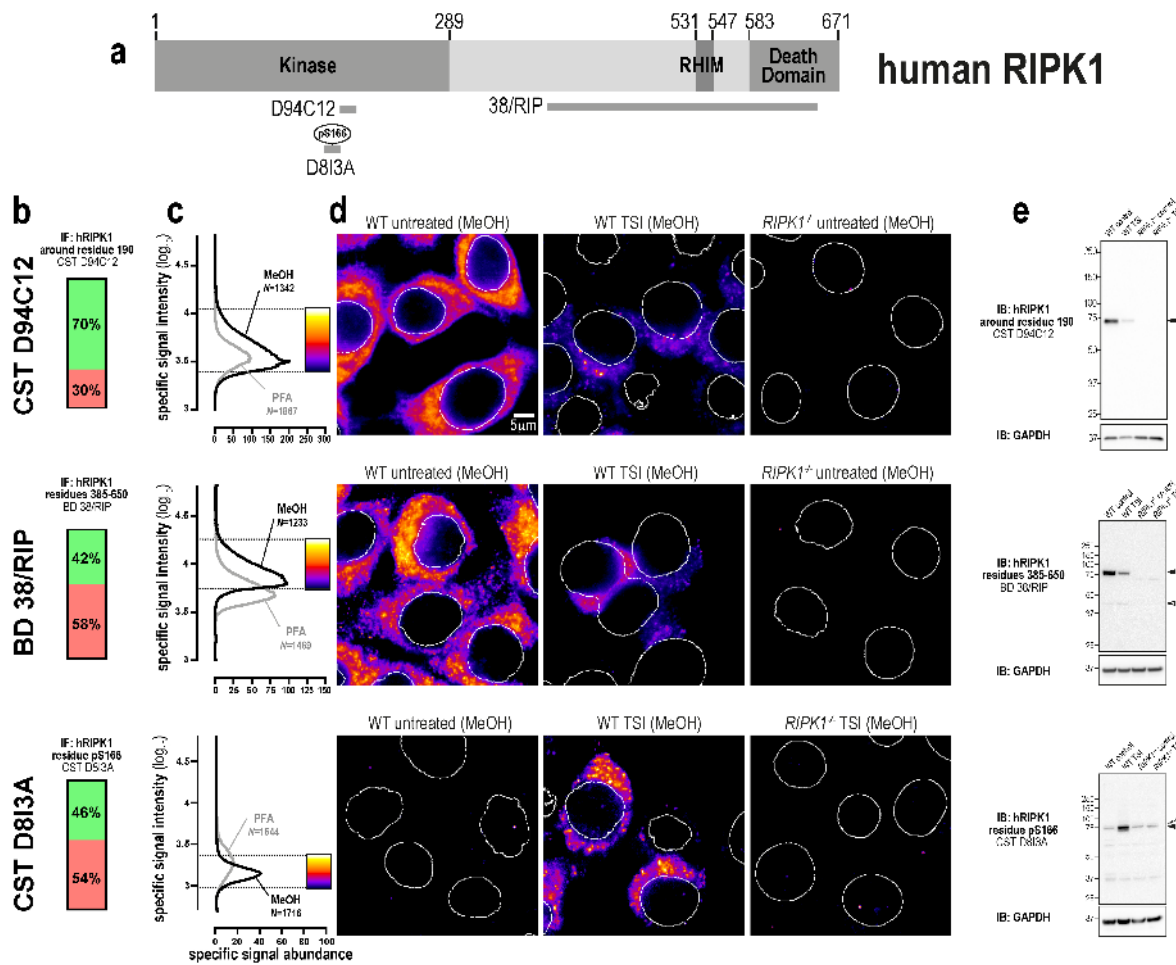
826 **Figure 2: Better antibodies are needed for imaging human RIPK3.**

827 **a** Human RIPK3 domain architecture showing the immunogens or epitopes for the tested anti-RIPK3
828 antibodies. **b** Quantitation of the percentage of gated signals for the tested RIPK3 antibodies. **c**
829 Quantitation of specific signal abundance produced by the tested RIPK3 antibodies on methanol-
830 fixed (MeOH) or paraformaldehyde-fixed (PFA) HT29 cells. The number of cells imaged (N) to
831 generate each signal-to-noise curve is shown. **d** Micrographs of immunofluorescent signals for the
832 tested RIPK3 antibodies on HT29 cells. As indicated by each pseudocolour look-up-table, only
833 immunosignals within the respective gate in panel **c** were visualised. Data are representative of n=3
834 (Cell Signaling Technology clone D6W2T and in-house clone 1H2) and n=2 (ProSci 2283, Novus
835 Biological NBP2-24588 and MAB7604/clone 780115) independent experiments. Nuclei were
836 detected by Hoechst 33342 staining and are demarked by white outlines in micrographs. **e**
837 Immunoblot using the tested RIPK3 antibodies against wild-type and *RIPK3*^{-/-} HT29 cell lysates.
838 Closed arrowheads indicate the main specific band. Open arrowheads indicate other specific bands
839 of interest. Immunoblots were re-probed for GAPDH as loading control.

840

841

Figure 3



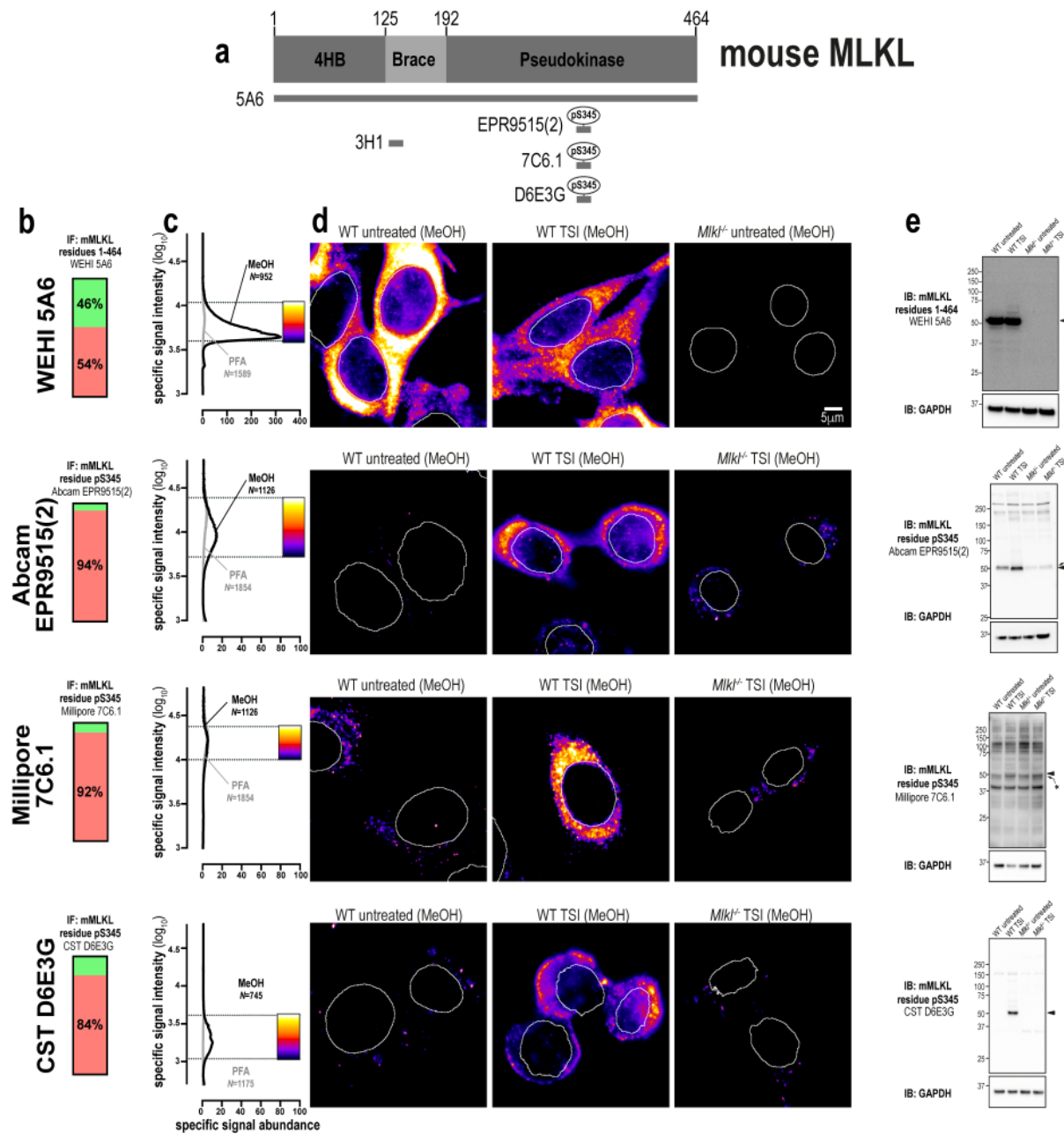
842

843 **Figure 3: Three specific antibodies for imaging endogenous human RIPK1.**

844 **a** Human RIPK1 domain architecture showing the immunogens or epitopes for the tested anti-RIPK1
 845 antibodies. **b** Quantitation of the percentage of gated signals for the tested RIPK1 antibodies. **c**
 846 Quantitation of specific signal abundance produced by the tested RIPK1 antibodies on methanol-
 847 fixed (MeOH) or paraformaldehyde-fixed (PFA) HT29 cells. The number of cells imaged (N) to
 848 generate each signal-to-noise curve is shown. **d** Micrographs of immunofluorescent signals for the
 849 tested RIPK1 antibodies on HT29 cells. As indicated by each pseudocolour look-up-table, only
 850 immunosignals within the respective gate in panel c were visualised. Data are representative of n=2
 851 (Cell Signaling Technology clones D94C12 and D8I3A, BD Transduction laboratories clone 38/RIP)
 852 independent experiments. Nuclei were detected by Hoechst 33342 staining and are demarked by

853 white outlines in micrographs. e Immunoblot using the tested RIPK1 antibodies against wild-type
854 and *RIPK1*^{-/-} HT29 cell lysates. Closed arrowheads indicate the main specific band. Open arrowheads
855 indicate other specific bands of interest. Asterisks indicate non-specific bands that could otherwise
856 confound data interpretation. Immunoblots were re-probed for GAPDH as loading control.
857
858

Figure 4



859

860 **Figure 4: A new monoclonal antibody to image endogenous mouse MLKL.**

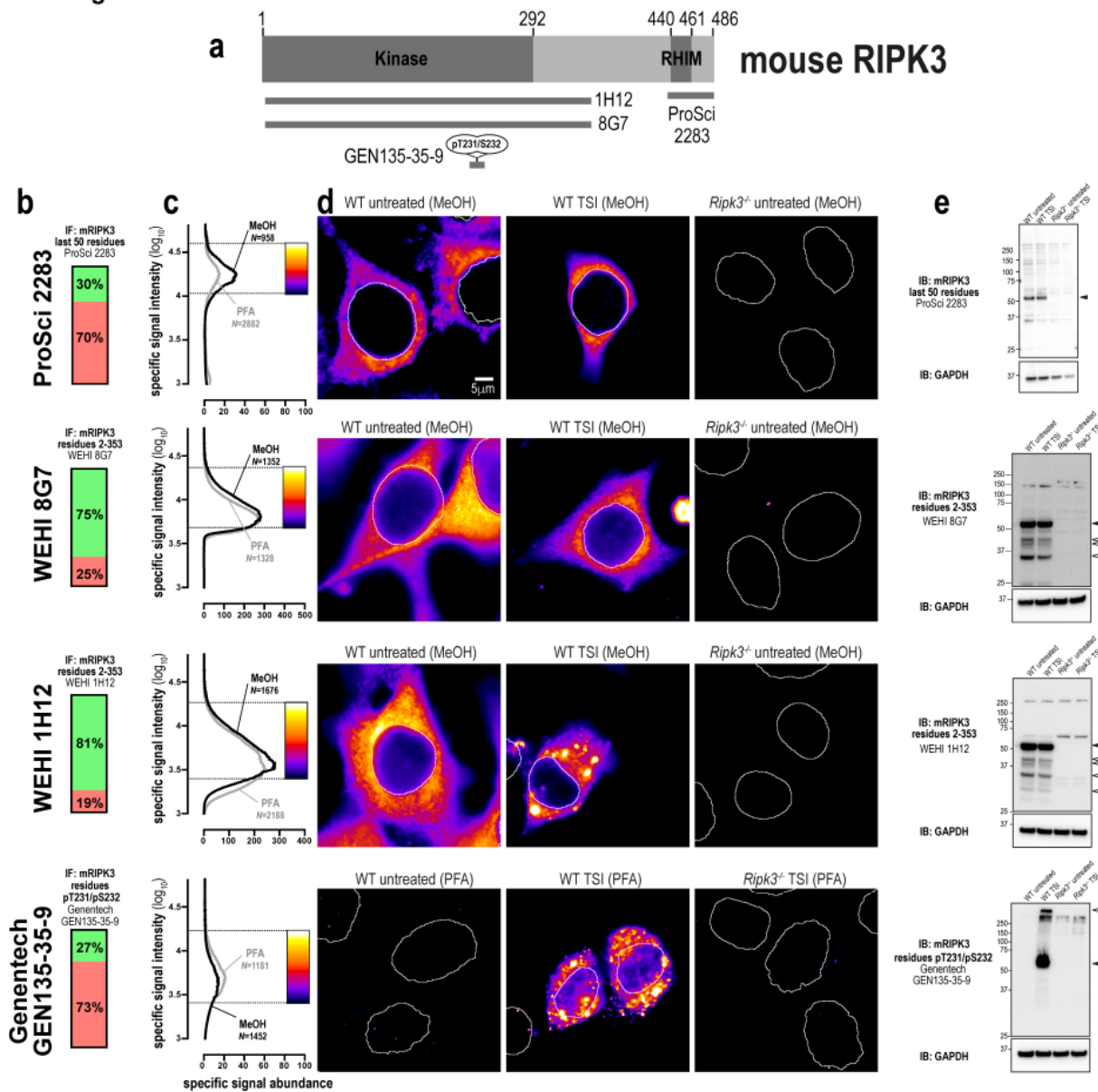
861 **a** Mouse MLKL domain architecture showing the immunogens or epitopes for the tested anti-MLKL
862 antibodies. **b** Quantitation of the percentage of gated signals for the tested MLKL antibodies.
863 **c** Quantitation of specific signal abundance produced by the tested MLKL antibodies on methanol-
864 fixed (MeOH) or paraformaldehyde-fixed (PFA) MDFs. The number of cells imaged (N) to generate
865 each signal-to-noise curve is shown. **d** Micrographs of immunofluorescent signals for the tested

866 MLKL antibodies on MDFs. As indicated by each pseudocolour look-up-table, only immunosignals
867 within the respective gate in panel **c** were visualised. Data are representative of n=3 (in-house clone
868 5A6) and n=2 (Abcam clone EPR9515(2), Millipore MABC1158/clone 7C6.1 and Cell Signaling
869 Technology clone D6E3G) independent experiments. Nuclei were detected by Hoechst 33342
870 staining and are demarked by white outlines in micrographs. **e** Immunoblot using the tested MLKL
871 antibodies against lysates from wild-type and *Mlkl*^{-/-} MDFs. Closed arrowheads indicate the main
872 specific band. Asterisks indicate non-specific bands that could otherwise confound data
873 interpretation. Immunoblots were re-probed for GAPDH as loading control.

874

875

Figure 5



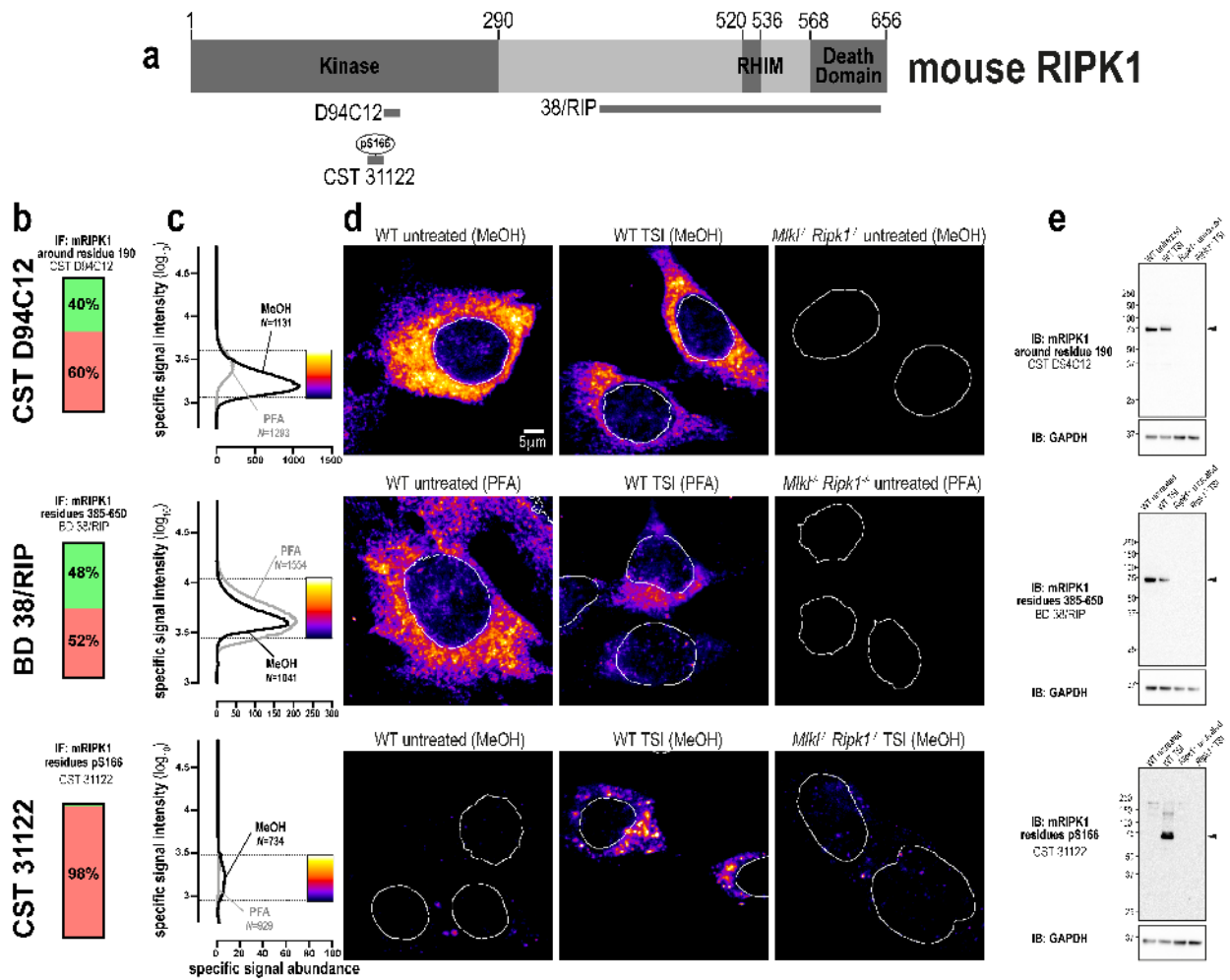
876

877 **Figure 5: Unlike human RIPK3, mouse RIPK3 is highly amenable to detection by**
 878 **immunofluorescence and immunoblotting.**

879 **a** Mouse RIPK3 domain architecture showing the immunogens or epitopes for the tested anti-RIPK3
 880 antibodies. **b** Quantitation of the percentage of gated signals for the tested RIPK3 antibodies. **c**
 881 Quantitation of specific signal abundance produced by the tested RIPK3 antibodies on methanol-
 882 fixed (MeOH) or paraformaldehyde-fixed (PFA) MDFs. The number of cells imaged (N) to generate
 883 each signal-to-noise curve is shown. **d** Micrographs of immunofluorescent signals for the tested

884 RIPK3 antibodies on MDFs. As indicated by each pseudocolour look-up-table, only immunosignals
885 within the respective gate in panel **c** were visualised. Data are representative of n=3 (in-house clone
886 8G7 and Genentech clone GEN135-35-9) and n=2 (ProSci 2283, in-house clone 1H12) independent
887 experiments. Nuclei were detected by Hoechst 33342 staining and are demarked by white outlines in
888 micrographs. **e** Immunoblot using the tested RIPK3 antibodies against lysates from wild-type and
889 *Ripk3*^{-/-} MDFs. Closed arrowheads indicate the main specific band. Open arrowheads indicate other
890 specific bands of interest. Immunoblots were re-probed for GAPDH as loading control.
891
892

Figure 6



893

894 **Figure 6: Three specific antibodies for imaging endogenous mouse RIPK1.**

895 **a** Mouse RIPK1 domain architecture showing the immunogens or epitopes for the tested anti-RIPK1

896 antibodies. **b** Quantitation of the percentage of gated signals for the tested RIPK1 antibodies

897 Quantitation of specific signal abundance produced by the tested RIPK1 antibodies on methanol-

898 fixed (MeOH) or paraformaldehyde-fixed (PFA) MDFs. The number of cells imaged (N) to generate

899 each signal-to-noise curve is shown. **d** Micrographs of immunofluorescent signals for the tested

900 RIPK1 antibodies on MDFs. As indicated by each pseudocolour look-up-table, only immunosignals

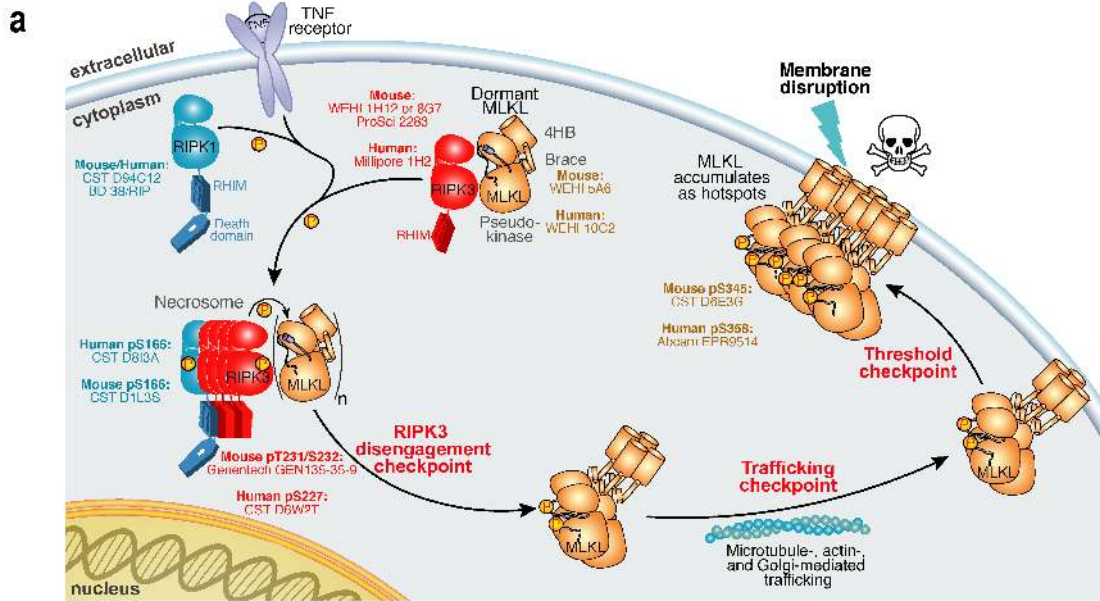
901 within the respective gate in panel **c** were visualised. Data are representative of n=2 (Cell Signaling

902 Technology clones D94C12 and 31122, and BD Transduction Laboratories clone 38/RIP)

903 independent experiments. Nuclei were detected by Hoechst 33342 staining and are demarked by

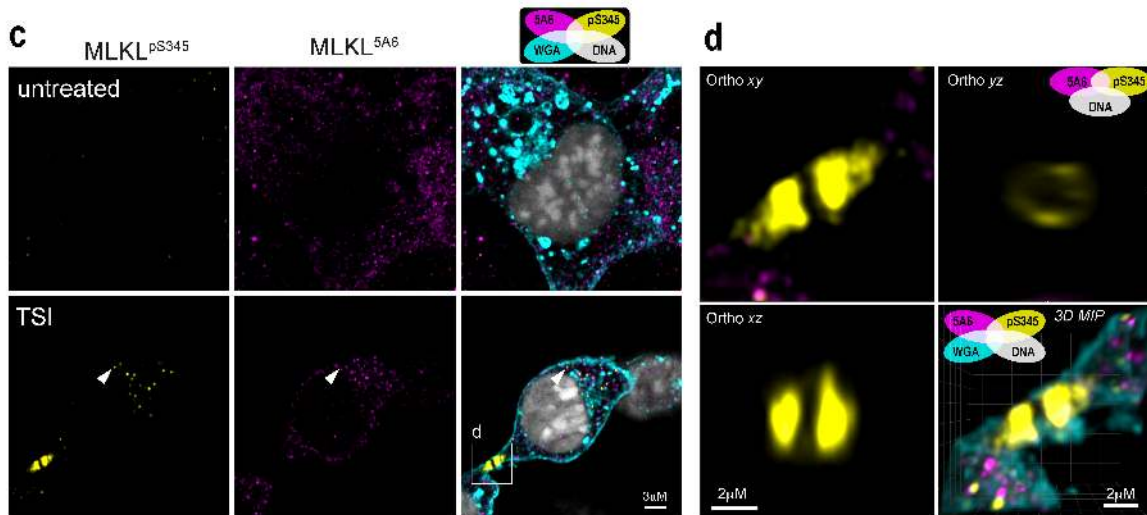
904 white outlines in micrographs. e Immunoblot using the tested RIPK1 antibodies against lysates from
905 wild-type and *Ripk1*^{-/-} MDFs. Closed arrowheads indicate the main specific band. Open arrowheads
906 indicate other specific bands of interest. Immunoblots were re-probed for GAPDH as loading control.
907
908

Figure 7



b

	mouse cells			human cells	
	cocktail #1	cocktail #2	cocktail #3	cocktail #4	cocktail #5
channel #1 (detected with fluorescent anti-rat IgG)	MLKL (clone 5A6) or RIPK3 (clone 8G7/1H12)	MLKL (clone 5A6) or RIPK3 (clone 8G7/1H12)	MLKL (clone 5A6) or RIPK3 (clone 8G7/1H12)	MLKL (clone 10C2) or RIPK3 (clone 1H2)	MLKL (clone 10C2) or RIPK3 (clone 1H2)
channel #2 (detected with fluorescent anti-rabbit IgG)	phospho-MLKL (clone D6E3G)	phospho-RIPK3 (clone GEN135-35-9)	phospho-RIPK1 (CST 31122)	phospho-MLKL (clone EPR9514)	phospho-RIPK1 (clone D8I3A)
channel #3 (detected with fluorescent anti-mouse IgG)	RIPK1 (clone 38/RIP)	RIPK1 (clone 38/RIP)	RIPK1 (clone 38/RIP)	RIPK1 (clone 38/RIP)	RIPK1 (clone 38/RIP)
channel #4 (suggested counterstains)	DNA (Hoechst 33342), membranes (biotinylated wheat germ agglutinin added 10 minutes before fixation then detected with fluorescent streptavidin), microtubules (anti-tubulin immunofluorescence with Cytoskeleton Inc. # ATN02 then detection with fluorescent anti-sheep IgG), or early endosomes (biotinylated transferrin added 10 minutes before fixation then detected with fluorescent streptavidin)				



909

910 **Figure 7: Optimised antibody cocktails for visualising endogenous necroptotic signaling in fixed**

911 **human and mouse cells.**

912 **a** Cartoon summary of the currently-understood chronology of TNF-induced necroptosis.
913 Recommendations of validated antibodies for immunostaining various steps in the necroptotic
914 pathway are provided. **b** Summary of validated antibody cocktails and counterstains that can be
915 multiplexed to examine endogenous necroptotic signaling in fixed human and mouse cells. Successful
916 detection of specific signals relies on fixation in methanol, rather than crosslinking fixatives such as
917 paraformaldehyde. **c** Two-dimensional Airyscan micrographs of Wheat Germ Agglutinin (WGA)-
918 stained membranes, Hoechst-stained DNA and anti-MLKL immunosignals from clone 5A6 and clone
919 D6E3G on methanol-fixed wild-type MDFs that had been left untreated or TSI-treated for 60min.
920 Arrowhead exemplifies the small clusters of MLKL that form during necroptosis. The box indicates
921 the junctional accumulation of phospho-MLKL. **d** Three-dimensional orthogonal projections and
922 maximum intensity projection (MIP) of the boxed region from panel **c** showing a ring-like structure
923 adopted by phospho-MLKL at the WGA-stained plasma membrane. Accompanied by Supplementary
924 Video 1.